RSC Advances

PAPER

View Article Online
View Journal | View Issue

Cite this: *RSC Adv.*, 2024, **14**, 27042

Orthorhombic–tetragonal phase coexistence and enhanced piezoelectric properties at room temperature in Zn and Ta modified $(Ba_{0.95}Ca_{0.05})(Zr_{0.05}Ti_{0.95})O_3$ ceramics through the synergistic effect of lattice distortion

Nabil Dhifallah, * Mohamed Amin Hentati and Hamadi Khemakhem

This study provides a fundamental understanding of the enhanced piezoelectric properties in ABO_3 perovskite based lead-free piezoelectric materials. For this we synthesized $(Ba_{0.95}Ca_{0.05})(Zr_{0.05}Ti_{0.95-x}(Zn_{1/3}Ta_{2/3})_x)O_3$((1 − *x*)BCZT−(*x*)ZT) (*x* = 0.00, 0.005, 0.01, and 0.02) solid solutions exhibiting high piezoelectric response. The (1 − *x*)BCZT−*x*ZT materials are synthesized by a high-temperature solid-state ceramic reaction method by varying *x* in the full range (*x* = 0.00–0.02). In-depth exploratory research is performed on the structural, dielectric, ferroelectric, and piezoelectric properties of (1 − *x*)BCZT−(*x*)ZT ceramics. The formation of perovskite structure for all ceramics without the presence of any impurity phases is confirmed by X-ray diffraction (XRD) analyses, which also reveals that the Ca^{2+}, Zr^{4+}, Zr^{2+} and Ta^{5+} are well dispersed within the $BaTiO_3$ lattice. For all (1 − *x*)BCZT−(*x*)ZT ceramics, thorough investigation of phase formation and phase-stability using XRD, Rietveld refinement, Raman spectroscopy, and temperature-dependent dielectric measurements provide conclusive evidence for the coexistence of orthorhombic + tetragonal (*Amm*2 + *P*4*mm*) phases at room temperature. The steady transition of *Amm*2 crystal symmetry to *P*4*mm* crystal symmetry with increasing *x* content is also demonstrated by Rietveld refinement data and related analyses. The *c*/*a* ratio of the tetragonal phase greatly influenced the electric properties of the ceramics. The *c*/*a* ratio of the tetragonal phase increases from 1.0112 for *x* = 0 to 1.0157 for *x* = 0.005 and subsequently decreases to 1.0038 for *x* = 0.02. When the *c*/*a* of the tetragonal phase reaches its maximum value, the ceramic with *x* = 0.005 has the best piezoelectricity ($d_{33} \sim 297$ pC N^{-1}). The calculated degree of relaxation (γ) increases with the increase in BZT content, indicating that the BCZT–*x*BZT ceramics are ferroelectric materials with diffuse phase transition. Main dielectric, piezoelectric and ferroelectric parameters of (1−*x*)BCZT–*x*ZT ceramics were optimized around *x* = 0.005 with a high piezoelectric coefficient (d_{33} = 297 pC N^{-1}), a remnant polarization (P_r = 7.58 μC cm^{-2}), spontaneous polarization (P_s = 10.25 μC cm^{-2}) and a high dielectric constant (ε_{max,T^c} = 4449 at T_c and 2330 near RT) at 1 kHz, indicating promising applications for lead-free piezoelectric ceramics.

Received 22nd May 2024
Accepted 14th August 2024

DOI: 10.1039/d4ra03784g

rsc.li/rsc-advances

1. Introduction

Lead zirconate titanate (PZT) based piezoelectric ceramics have played a role in the piezoelectric applications because of their outstanding piezoelectric properties and good temperature stability.[1,2] However, due to the toxicity of lead compounds, several research groups have focused on developing new lead-free alternative materials with comparable piezoelectric and electromechanical properties to their lead-based counterparts.[3,4] Barium titanate ($BaTiO_3$) is one of the most widely studied lead-free piezoelectric materials.[5,6] It has a relatively simple structure and show polymorphic phase transitions.[7] At atmospheric pressure, it undergoes structural phase transitions from cubic-to-tetragonal phase at 405 K, tetragonal-to-orthorhombic phase at 273 K, and finally orthorhombic-to-rhombohedral phase at 200 K. The high temperature cubic phase is paraelectric, and all low temperature phases are ferroelectric. The reported piezoelectric charge coefficient (d_{33}) of pure $BaTiO_3$ ceramic is 190 pC N^{-1}.[8] However, this value increases to as high as 420 and 300 pC N^{-1} in the vicinity of tetragonal-to-orthorhombic and orthorhombic-to-rhombohedral transition temperature, respectively.[9] This observation suggests that high piezoelectric coefficient can be achieved by bringing the T–O phase transition temperature near

Laboratory of Multifunctional Materials and Applications (LaMMA), University of Sfax, Faculty of Sciences of Sfax, Soukra Road PB 1171, Sfax, 3000, Tunisia. E-mail: dhifallahnabil@yahoo.fr

the room temperature with the help of a dopant or by making a solid solution.[5] Yu *et al.*[10] has observed optimum piezoelectric properties from 5 mol% Zr^{4+} substitution in $BaTiO_3$, *i.e.*, $Ba(Zr_{0.05}Ti_{0.95})O_3$. The tetragonal-to-orthorhombic phase transition temperature is nearly 58 °C in this composition having orthorhombic symmetry at room temperature (27 °C). For this composition, the reported tetragonal-to-orthorhombic phase transition temperatures are nearly 331 K having orthorhombic symmetry at room temperature (300 K). Recently, Li *et al.*.[11] have shown that the piezoelectric properties of $Ba(Zr_{0.05}Ti_{0.95})O_3$ can further be improved by doping with calcium (Ca^{2+}). The key advantage of calcium doping is that it decreases the tetragonal-to-orthorhombic and orthorhombic-to-rhombohedral phase transition temperatures of $Ba(Zr_{0.05}Ti_{0.95})O_3$ without affecting the cubic-to-tetragonal transition temperature. Therefore, tailoring of tetragonal-to-orthorhombic transition temperature can be achieved without lowering the cubic-to-tetragonal transition temperature. We have recently investigated dielectric, piezoelectric and structural behaviour of $(Ba_{1-x}Ca_x)(Zr_{0.05}Ti_{0.95})O_3$ ceramic, showing a phase transition T_{O-T} at RT for $x = 0.05$, and revealing high electro-mechanical properties[11] and thermal stability of piezoelectric coefficients[12] and has a Curie temperature ($T_C \sim 120$ °C) higher than that of $Ba_{0.85}Ca_{0.15}Ti_{0.9}\ Zr_{0.1}O_3$ ($T_C \sim 93$ °C).[13] It is, therefore, expected that this ceramic will give a better electro-caloric effect.

Current methods to optimize the performance of piezoelectric ceramics include the construction of morphotropic phase boundaries (MPBs),[14,15] ionic doping,[16] and the introduction of local structural heterogeneities.[16,17] Tracing back to the source, the essence of these methods is based on ease of domain flipping during polarization, which is influenced by the deformation of oxygen octahedra in the perovskite structures (ABO_3). It is found that most stable octahedral structures are not ideal positive octahedral structures, having instead undergone distortions that change the symmetry and energy band structure of the perovskite structures while bringing about entirely new properties. Octahedral distortion and displacement of A/B sites are the origins of spontaneous polarization of ferroelectrics, which directly affects the piezoelectric response behavior. Li *et al.*[18] have confirmed that the high piezoelectric properties originate from the high lattice distortion of textured ceramics under the action of applied electric fields, providing an intrinsic contribution to the piezoelectric response. Wang *et al.*[19] have induced octahedral tilt by $BaSnO_3$ doping with a large tolerance factor, rendering excellent piezoelectricity ($d_{33} \sim 354$ pC N^{-1}) and high thermal stability (20–100 °C). Therefore, it is feasible to obtain high piezoelectric properties and good thermal stability by the rational arrangement of the crystal structure. It has been shown that effective doping could bring suitable octahedral distortion.[20,21] The octahedral distortion can be explained by the Juhn–Teller effect (JTE), which reveals the conformational deformation of the electronic cloud of a nonlinear molecule under certain circumstances, leading to a further decrease in the system energy by reducing the symmetry and orbital simplicity of the molecule.[22] When different ions are doped into the ceramic lattice, they render different hybridization effects with surrounding atoms because of the different electronegativity and ionic radii, influencing the lattice distortion of ion-doped ceramics.

In addition to XRD, Raman spectroscopy has also been used to determine the structural modifications and the phase transitions in perovskite-like materials, including the $BaTiO_3$ family,[23] oxide spinel ferrites,[24] and was established as a powerful tool to study correlated materials.[25] Numerous Raman studies engaged in the correlation of the observed Raman modes to the presence of Jahn–Teller (JT) distortions in the manganite system.[26,27] This technique is non-destructive and versatile, allowing measurements with adjusted spatial resolution and under different conditions of temperature, pressure, and electric field, in order to enhance the understanding about chemical bonding and local distortion of BO_6 octahedra, causing different macroscopic responses.[28–31] For example, Buscaglia *et al.*[29] identified the ferroelectric-to-paraelectric transition in $Ba(Zr,Ti)O_3$ compounds by using temperature-dependent Raman spectroscopy. More recently, Coondoo *et al.*[32] reported a detailed temperature-dependent Raman investigation only of a $0.5Ba(Ti_{0.8}Zr_{0.2})O_3$–$0.5(Ba_{0.7}Ca_{0.3})TiO_3$ ceramic, identifying the phase transitions by using the intensity, frequency position and width of the main stretching vibrational mode of the bond in [TiO_6] octahedra. In addition, for high-power applications, defect dipoles play a unique and important role in achieving a high piezoelectric coefficient d_{33}. As we all know, the introduction of acceptor-doped piezoelectric ceramics leads to the "hardening" effect.[33,34] The acceptor ion possesses a lower valence status compared to the substituted ion, as in the case of ZnO-doped BCZT.[35,36] Consequently, defect dipoles are formed through charge compensation and external electric field to reduce the electrostatic field and create a pinning effect. B-site off centering displacement controls the tetragonality and is only weakly dependent on the A-site displacements.[37] This implies the contribution of local structural distortions due to B-site substitutions towards enhanced piezoelectric response. In order to avoid the degradation of electrical performance, compensation for the B-site vacancies is urgently required. In the modication of BCZT-based ceramics, Ta with high Pauling electronegativity leads to significant improvements in the piezoelectric performance.[38] When donor ions were added to ceramics, the oxygen vacancy concentration was restricted. As a result, the pinning of domains is reduced and the domain wall motion is promoted, which improves the electrical properties of ceramics.

In this work, a series of Zn an Ta will be introduced $(Ba_{0.95}Ca_{0.05})(Zr_{0.05}Ti_{0.95})O_3$ (BCZT) ceramics, with the aim of achieving high piezoelectric performance. We have introduced different amounts of ZT, as a dopant, in the BCZT system to investigate the relationship between tetragonality degree (c/a), microstructure, lattice parameters, phase content and piezoelectric properties. Understanding this relationship is an important basis for modification operations. The successful preparation of ZT-doped BCZT piezoelectric ceramics will provide guidance to further improve the piezoelectric properties of different piezoelectric materials.

2. Experimental procedures

The $(Ba_{0.95}Ca_{0.05})(Zr_{0.05}Ti_{0.95-x}(Zn_{1/3}Ta_{2/3})_x)O_3$ ($x = 0.00$, 0.005, 0.01, and 0.02) (BCZT–xZT) ceramics were prepared by the conventional solid-state reaction technique. The reagent grade materials of $BaCo_3$, $CaCo_3$, TiO_2, ZrO_2, ZnO and Ta_2O_5 powders were weighed as starting powders according to the nominal stoichiometric ratio. All these materials were preheated at 150 °C for 4 h, weighted; mixed, and then grounded in an agate mortar using ethanol for 4 h.

Then, the mixed powder was dried and calcined at 1250 °C for 12 h. Then, the obtained chamottes were remixed for 2 h with 5% by mass of polyvinylidene alcohol (PVA). After grinding, the mixture of powders was pressed 50 MPa into a pellet of 8 mm of diameter and 1 mm of thickness. After binder release at 600 °C for 4 h, the resulting disk ceramics were sintered at 1500 °C for 4 h. The phase structures of sintered ceramics were detected by X-ray diffraction (XRD, Panalytical X′Pert, using Cu-Kα ($\lambda \sim 1.5406$ Å) radiation). The microstructure was examined by means of scanning electron microscopy analysis (SEM: JEOL SEM JCM 7000). The average grain size distribution was evaluated using Image J software. Raman spectra of sintered samples were recorded from 50 to 1000 cm^{-1} in a micro-Raman Spectrometer (LABRAM HR-800), working in a backscattering configuration, equipped with an He^+ ion ($\lambda = 633$ nm) laser. The spectral resolution of the system was 3 cm^{-1}.

Temperature dependence of dielectric properties of the ceramic samples was measured using an LCR meter (Agilent HP4284) in the temperature range from 300 K to 450 K and at different frequencies (1 kHz–1 MHz). The (P–E) loop was computed at a frequency of 15 Hz at room temperature with an applied electric field of 30 kV cm^{-1}). The ferroelectric hysteresis loops were recorded using a high voltage amplifier with a current amplifier (GX 320 matrix) at the frequency of 15 Hz at room temperature under an applied electric field of 30 kV cm^{-1}. The value of the piezoelectric constant (d_{33}) was measured using Polyc quasi-static piezoelectric constant d_{33} meter.

3. Results and discussion

Fig. 1(a) shows the X-ray diffraction patterns of the (1−x)BCZT–xZT ceramics measured at room temperature, which all exhibit a pure perovskite structure without any trace of impurity phase, suggesting that both Ca, Zr, Zn and Ta diffuse into the host lattice to form a solid solution. The diffraction peaks at $x = 0$ correspond well with PDF#81-2200,[39] suggesting that the crystalline structure of sample orthorhombic symmetry,[40] in which two peaks of $(022)_O$ and $(200)_O$ are visible around 44.84°–45.09° in the enlarged Fig. 1(b).

Meanwhile, the coexistence of tetragonal and orthorhombic phases for $x = 0.005$, 0.010 and 0.02 at RT, confirms the morphotropic phase boundary (MPB) nature of these compositions. In fact, to observe the (200) peaks clearly, XRD patterns of the (1 − x)BCZT–xZT ceramics in the 2θ range of 44.84°–45.09° are shown in Fig. 1(c)–(e), respectively. The Voigt function is used to separate the overlapped (200) lines. Concerning the peaks, they can be regarded as the mixture of the three peaks. The splitting of two peaks (002) and (200) corresponds to the tetragonal phase; the orthorhombic symmetry is indicated by an obvious peak (022). The radius of Zn^{2+} ($r = 0.74$, ionic radius) and Ta^{5+} ($r = 0.64$, ionic radius) is lightly greater than that Ti^{4+} ($r = 0.605$, ionic radius) and Zr^{4+} ($r = 0.72$, ionic radius).[41] That is why Zn^{2+} and Ta^{5+} occupying B site were added with Ti^{4+}.

The diffraction peaks of BCZT–xZT ceramics exhibits pure orthorhombic structure ($x = 0$) with obvious splitting of the (022)/(200) peaks at $\sim 2\theta = 44.84°$, this imply that ZT doping induces the lattice distortion and forms morphotropic phase boundary (MPB) at room temperature.[42,43] According to the report of the tolerance factors by Li *et al.*,[44] take Zn^{2+} ($r = 0.74$ Å) and Ta^{5+} ($r = 0.64$ Å) into consideration, it is concluded that Zn^{2+}/Ta^{5+} occupy B site, resulting in a change for the lattice parameter and oxygen vacancies. The oxygen vacancies contribute to the mass transport and improve the density during sintering process. These results confirm that the Zn^{2+}/Ta^{5+} partially enters the B site in the lattice and changes the crystal structure,[43,45] which affects that the peaks shift to higher angles.

To probe the structural transformations and provide a thorough analysis of phase formation and stabilization, we performed the Rietveld refinement of XRD patterns. Fig. 2(a)–(d) shows Rietveld fitted XRD patterns of (1 − x)BCZT–xZT materials with orthorhombic (*Amm*2) (PDF#81-2200) and tetragonal (*P*4*mm*) (PDF#05-0626) crystal structure. For $x = 0$, phase analyses reveal that the *Amm*2 phase percentage (68%) is larger than the *P*4*mm* phase (32%). However, as the amount of x (ZT-content) increases, the proportion of tetragonal phase symmetry gradually rises. This observation indicates that the ZT-concentration in the ceramics influences the specific phase formation and the sequence of phase-transformation. The refined structural parameters, such as lattice parameters, respective phase percentages, are presented in Table 1. Rietveld refinement analyses clearly authenticate the coexistence of both the *Amm*2 (O) and *P*4*mm* (T) phases which can play a vital role in enhancing the piezoelectric properties.[44–46] Thus, combined XRD and Rietveld refinement analyses demonstrate the ability to control the structure and phase, which in turn influence the properties and performance, of resulting (1 − x)BCZT–xZT materials.[47,48]

According to the XRD results, the average crystallite size D and the constraint ε of the (1 − x)BCZT–xZT materials could be estimated using the Williamson–Hall (W–H) approach:[49]

$$\beta \cos\theta = \frac{k\lambda}{D} + 4 \sin\theta$$

where β is the full width at half-maximum intensity (FWHM) of the diffraction peak, θ is the diffraction angle, k is the shape factor taken here to be equal to 0.9, and λ is the wavelength of Cu-Ka radiation, here equal to 1.540 Å. Also, $\frac{k\lambda}{D}$ represents the enlargement due to the crystallite size and $4\varepsilon \sin\theta$ represents the enlargement due to the distortion of the crystal lattice. The linear plot of $\beta \cos\theta$ *versus* $4 \sin\theta$ yields the intercept as the crystallite size and the slope as the strain, as shown in Fig. 3(a)–(d). The observed positive slope confirmed the tensile

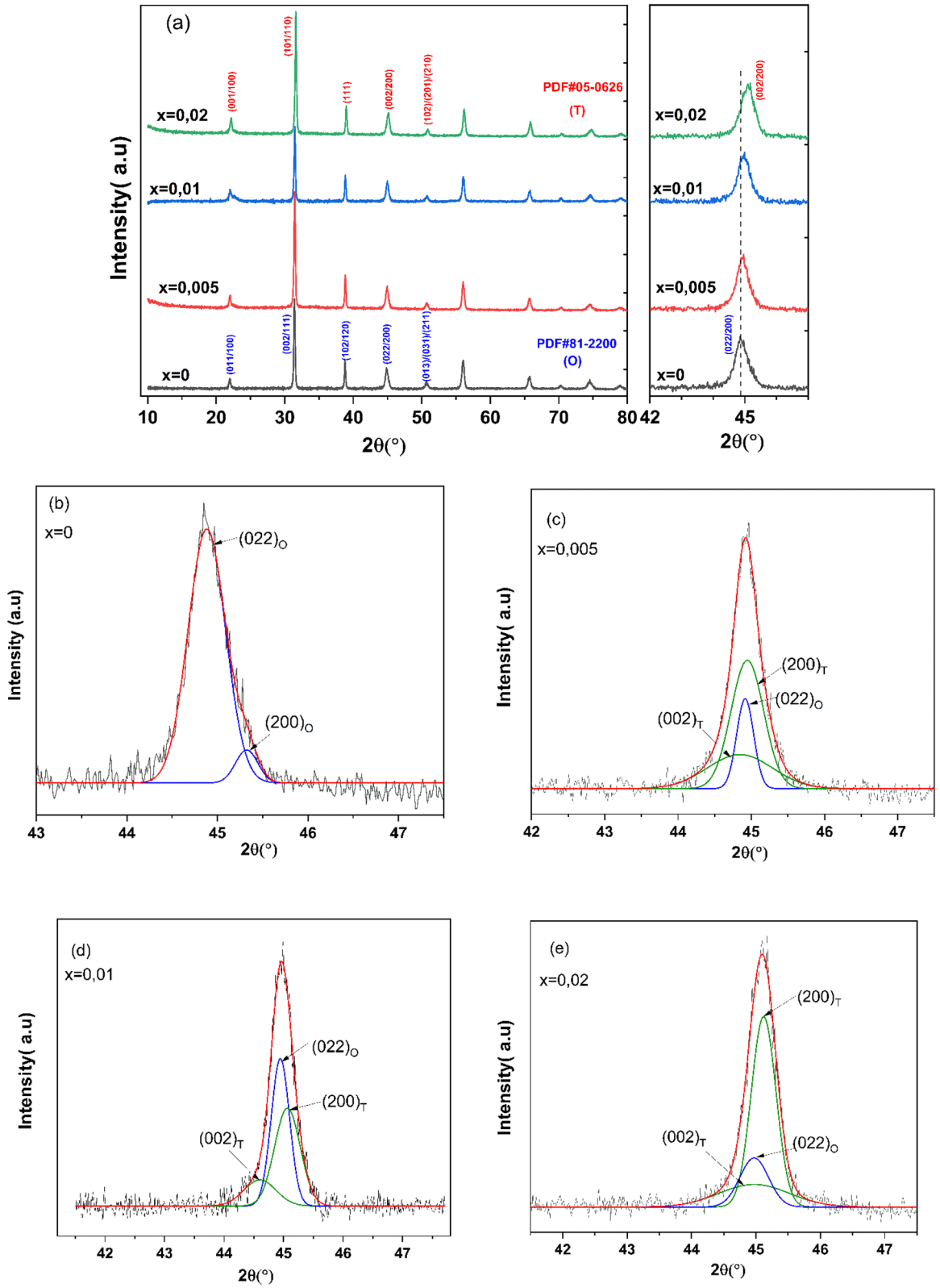

Fig. 1 (a) X-ray diffraction patterns of the BCZT–*x*BZT ceramics. (b)–(e) X-ray diffraction patterns and fitting curves in the 2θ range of 44°–46°.

strain experienced in the smaller sized grain. The values of D and ε were calculated from the y-intercept and slope of the fitted line, respectively, and are presented in Table 1. These values of lattice distortion were comparable with those previously reported for the ABO_3 structure.[50]

Fig. 4(a)–(d) shows the SEM micrographs of the surface of the BCZT–xZT ceramics (x = 0, 0.005, 0.01, 0.02) including the

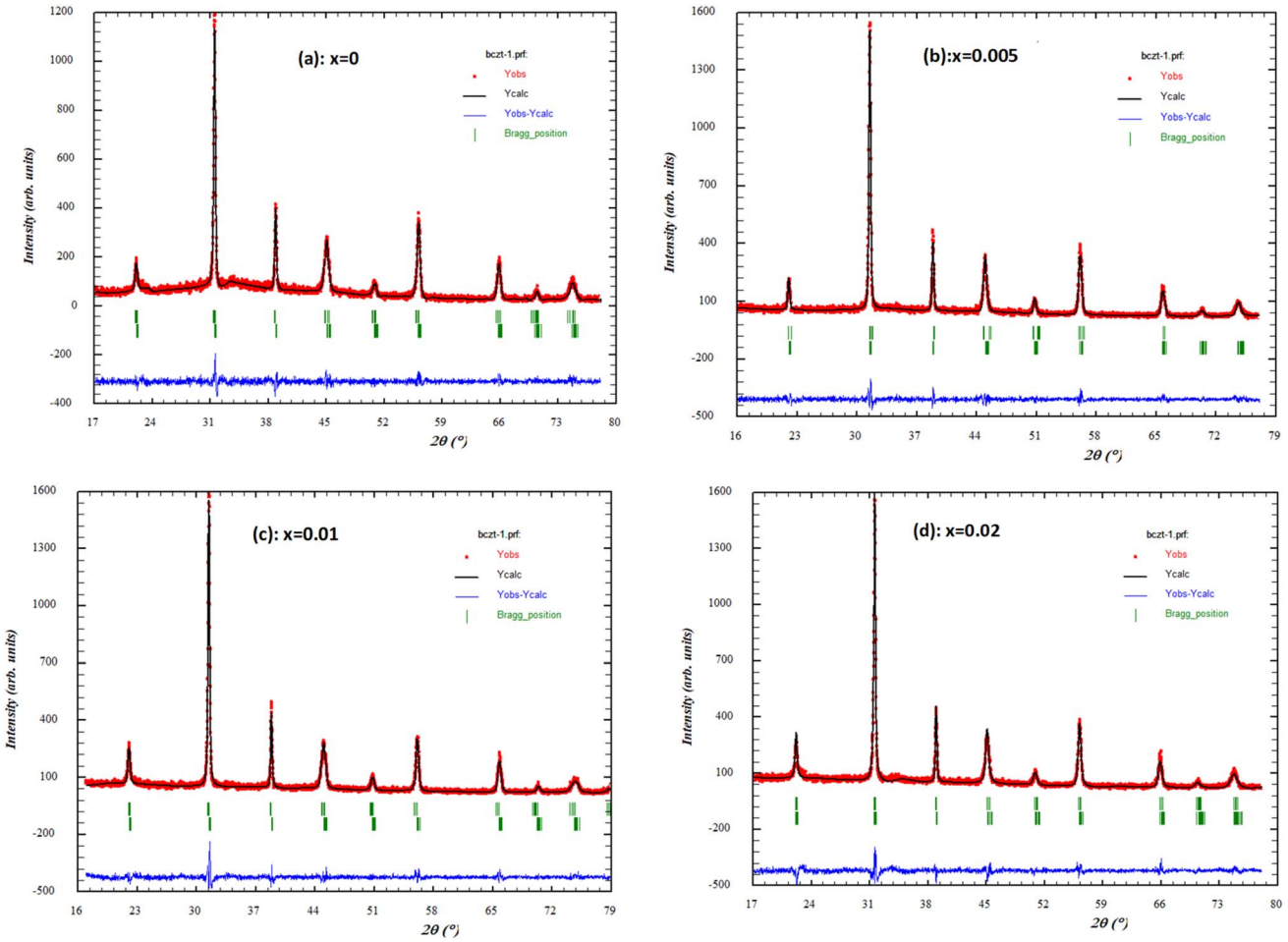

Fig. 2 Rietveld fitted XRD patterns of (1 − *x*)BCZT–(*x*)ZT samples. (a) $x = 0.0$; (b) $x = 0.005$; (c) $x = 0.01$; (d) $x = 0.02$.

histogram that illustrates the variation of grain size spectra for various *x* contents are shown in Fig. 4(e)–(h), respectively. It can be observed that all samples showed high density with low porosity and the grain size was gradually increased by increasing the BZT content. The BCZT ceramic has the smallest average grain size, 10.42 μm, without any addition of ZnO/Ta_2O_5.

Table 1 lists the density ρ and average grain size *g* of BCZT–*x*ZT ceramics. The pure BCZT ceramics possess lower density than that of samples with ZnO/Ta_2O_5 addition. For those BCZT ceramics doped ZnO/Ta_2O_5 less than $x = 0.005$, the density ρ and average grain size *g* increase with adding ZnO/Ta_2O_5. The average grain size *g* increased from 11.31 μm to 20.54 μm. The BCZT–0.005ZT ceramics shows the largest density ρ. However,

Table 1 Data of the density ρ, the average grain size *g* for the various BCZT–*x*ZT ceramics, structural parameters obtained from Rietveld refinement considering *Amm*2 + *P*4*mm* space group model for (1 − *x*)BCZT–(*x*)ZT materials and values of crystallite size *D* and microstrain ε

Parameters		$x = 0$	$x = 0.005$	$x = 0.01$	$x = 0.02$
Lattice constants (*a*, *b*, *c*) of	*a*	4 005 998	3.999910	400 502	400 208
orthorhombic (O) phase with space	*b*	3 993 685	4.004676	400 762	397 905
group, *Amm*2	*c*	402 678	4.024212	402 174	40 159
Lattice constants (*a*, *b*, *c*) of tetragonal (T)	*a*	4 004 152	398 249	398 753	400 208
phase with space group, *P*4*mm*	*b*	4 004 152	398 249	398 753	400 208
	c	4 049 344	404 934	40 426	401 753
c/*a* (*P*4*mm*)		101 129	101 572	101 381	100 386
Phase (%)	O	68	59	54	41
	T	32	41	46	59
Density ρ (g cm^{-3})		5.37	5.55	5.44	5.43
Average grain size *g* (μm)		11.31	20.54	15.36	13.78
Crystallite size *D* (nm)		5 753 278	3 677 825	343 203	3 573 557
Microstrain ε		1.1×10^{-3}	1.92×10^{-3}	1.47×10^{-3}	1.69×10^{-3}

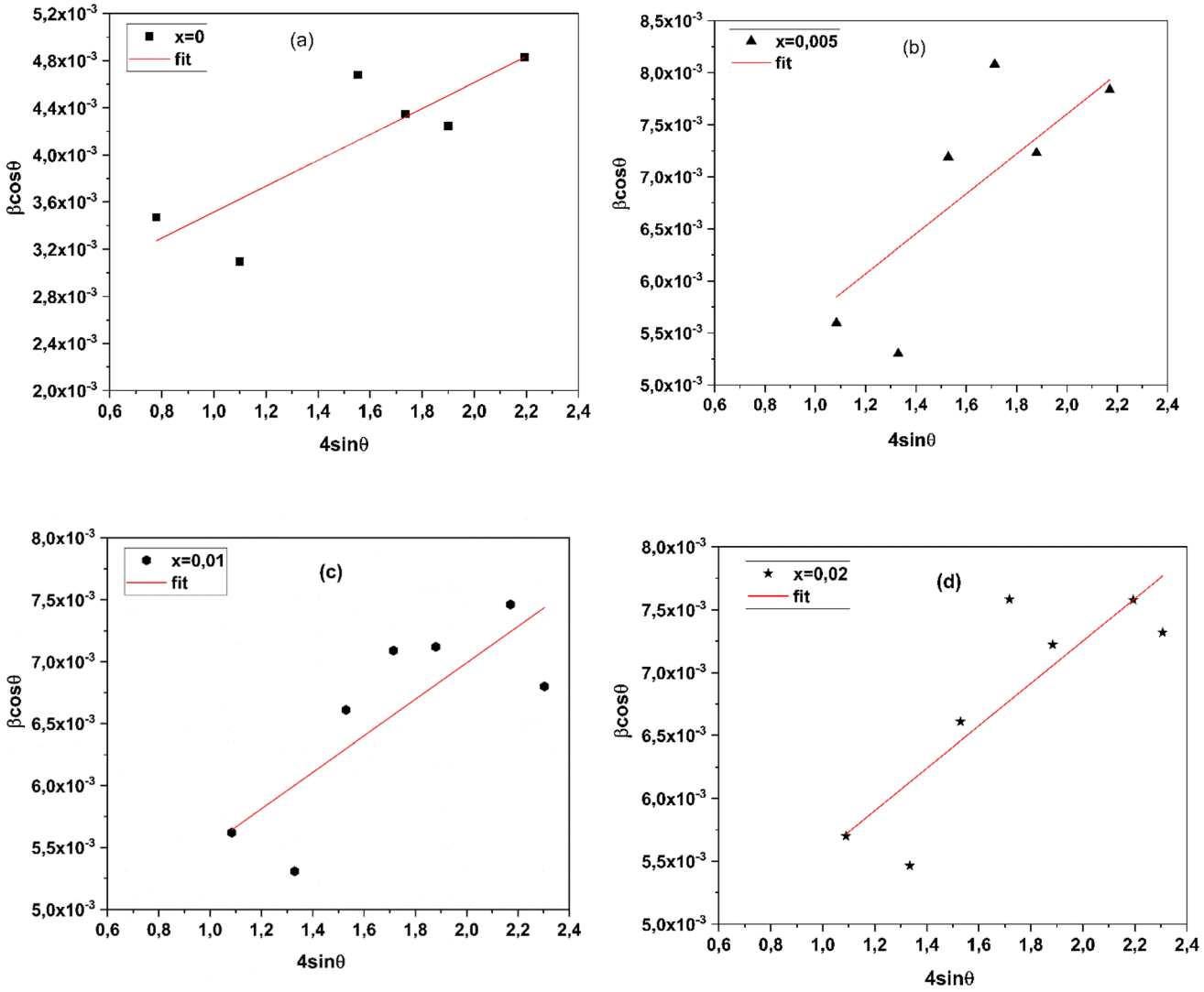

Fig. 3 (a–d) Presents Williamson–Hall plot of BCZT–ZT samples.

further doping the ZnO/Ta_2O_5 (>0.005) the density ρ and average grain size g decrease. However, when the concentration of BZT is greater than $x = 0.005$, the grains become much smaller, because ZnO/Ta_2O_5 may stockpile in the grain boundary and suppress the grain growth. According to Han's report,[51] the Zn^{2+}/Ta^{5+} substitution into the $(Ti)^{4+}$ site results in the generation of oxygen vacancy. Therefore, we believe that the grain growth of ZnO/Ta_2O_5-doped BCZT ceramics is due to the presence of oxygen vacancy that helps the mass transport.[52]

Raman spectroscopy is a nondestructive probe of the structure of ferroelectric materials owing to its sensitivity to local symmetry. Raman scattering also provides information about local heterogeneities related to compositional and structural disorder because of the shorter coherence length and time scale of phonons. Therefore, the Raman spectra of the BCZT–xZT system have been studied as a function of composition for realizing ZT doping effects to local heterogeneities structure of BCZT–xZT ceramics. The reduced intensity, corrected for the Bose–Einstein phonon population, was reckoned from stokes components of observed Raman scattering intensity, $I(\omega)$ as follows.[53]

$$I'(\omega) = \frac{I(\omega)}{\omega[n(\omega)+1]}$$

where, $n(\omega) = \frac{1}{e^{\left(\frac{\hbar\omega}{k_B T}\right)} - 1}$ represents the Bose–Einstein population factor, $\hbar$ and k_B indicate Dirac and Boltzmann constants, respectively.

The composition dependent Raman spectra measured at room temperature of the BCZT–xZT is shown in Fig. 5(a). The observed Raman spectra exhibit a similar profile of the pure $BaTiO_3$ (BT).[54,55] Therefore, the effective vibrational modes of BCZT–xZT ceramics are similar to that of pure BT. Pure BT is a typical ferroelectric material and it has tetragonal structure at room temperature. In the paraelectric cubic phase, the Raman modes of BT transform as the $3F_{1u} + F_{2u}$ irreducible presentations of the $Pm\bar{3}m$ symmetry. The F_{2u} mode is silent and F_{1u}

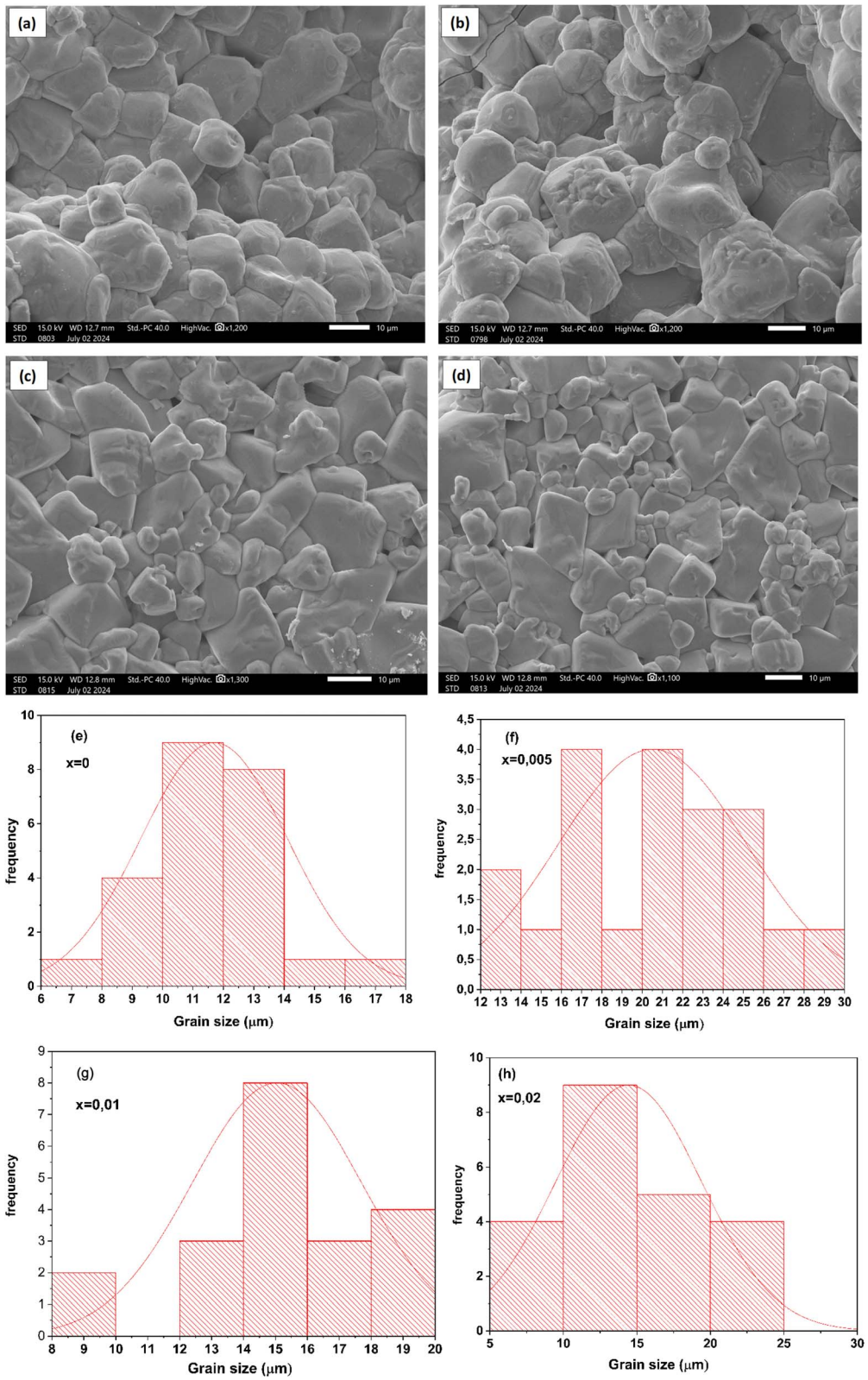

Fig. 4 (a)–(d) SEM images and (e)–(h) grain size distributions of BCZT–*x*ZT ceramics.

modes are only infrared active. Therefore, the Raman activity is not allowed in the paraelectric phase with perfect cubic symmetry. A ferroelectric tetragonal phase with *P*4*mm* symmetry has $3A_1$ and 3E modes, which comes from infrared active F_{1u} modes and one silent $(E + B_1)$ mode arises from F_{2u} mode. Each of the A and E modes splits into transverse optic

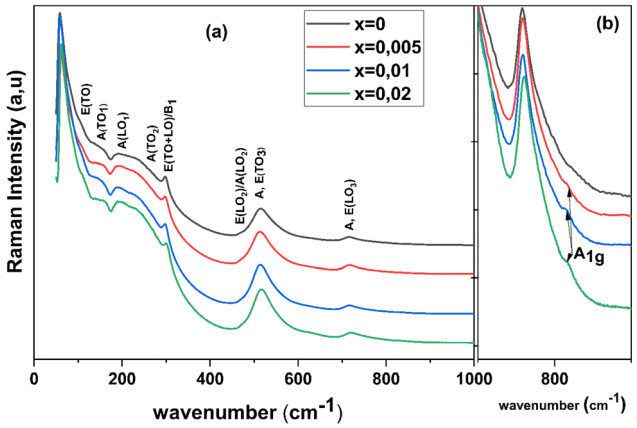

Fig. 5 Raman spectra recorded at RT for various compositions of BCZT–*x*ZT.

(TO) and longitudinal optic (LO) modes due to long-range electrostatic forces associated with lattice ionicity. The detailed mode symmetry assignments of $BaTiO_3$ are reported elsewhere.[56]

The spectrum includes all modes allowed by Raman selection rules; however, except for the forbidden prominent peak near 555 cm^{-1} and broadening of bands associated with compositional disordering. The otherwise strong spectral dip observed in BTO near 180 cm^{-1} (ref. 57) and understood as a result of the anti-resonance effect owing to anharmonic coupling among three A(TO) phonons, is less pronounced in the BCZT composition. Dominant A(TO) character is evident for the peaks observed near 265 cm^{-1} and 512 cm^{-1}; the former being associated with polar Ti–O vibrations while the latter is related to distortion in the TiO_4 plane and bending of the Ti ion and apical oxygen atoms. Another band at around 297 cm^{-1} assigned to a combined mode [B_1, E (TO + LO)] is also considered as a particular distinctive of the tetragonal phase. The Raman mode assignments are considered to be the same as those for pure $BaTiO_3$,[54,55] whereas a clear mode was labeled at 190 cm^{-1} for the all compounds and reported to be assigned to the A (LO) mode.[58,59] This band is reported to be more noticeable in the rhombohedral (R) and orthorhombic(O) phases, and it disappears in the tetragonal phase,[58–60] which suggests the coexistence of orthorhombic and tetragonal phases in accordance with the X-ray diffraction data. Generally, additional phonon modes appear owing to size effects, change in inter-atomic forces due to chemical substitution and high mechanical pressure which causes disorder in the position of Ti atoms that breaks the Raman selection rules.[61,62] The characteristic LO mode at ~716 cm^{-1} is due to the bending and stretching of BO_6 octahedra giving it a mixed A and E character. The appearance of an additional phonon mode at 755 cm^{-1}, is splitting of the LO mode attributed to the heavier B-site substitution.[63,64] The lower Raman band ~716 cm^{-1} corresponds to Ti–O stretching whereas the 755 cm^{-1} band represents Nb–O stretching.[65] In such system the vibration associated with two band modes do not couple due to their different chemical origin. The appearance of a mode at 755 cm^{-1} was considered as local counterpart of the A1(LO_3) mode appearing at 716 cm^{-1} in pure BCZT and is related to the internal deformation of the BO_6 octahedra due to the different cation substitutions on B site. The difference in the ionic radii of Zn^{2+} (0.74 Å) and Ta^{5+} (0.64 Å) substituted on Ti^{4+} (0.605 Å) site would give rise to elastic dipole like distortion in the surrounding region.[66] An alternative explanation for the occurrence of mode at 755 cm^{-1} was provided by Lazarevic *et al.*,[67] who claimed it to be due to the multiphonon process. The broad mode at ~829 cm^{-1} (A_{1g}) (in Fig. 5(b)) is an octahedral breathing-like mode resulting from the presence of two or more B-site species[68] and it may appear regardless of the presence or absence of a ferroelectric phase.[64] The B-site substituted by Ta^{5+} ions are more covalently bound to oxygen than Ti^{4+} ions and Zn^{2+} ions resulting in a strong off-centered axially perturbed octahedral crystal field. This perturbation can also be seen in A_{1g} (~829 cm^{-1}) modes of Raman spectra of BZT doped BCZT. This can be rationalized by considering that atomic positional disorder in general; and of niobium and copper in particular at the lower concentration of Zn^{2+} and Ta^{5+}. The disorder increases as the population of polar to non-polar phase evolves. The perturbation of nanopolar regions is higher with increased concentration of B-site transition metal ions. Raman analysis also indicates an increase in the spatial range to which local tetragonal distortions can propagate coherently with increase in B-site substitutions which in turns increases the mean free path of the phonons associated with polar distortions. It is interesting to note that such a small compositional changes substantially modulates the local dynamics and distortions favoring a piezoelectric response.[69]

It is well established fact that during polymorphic phase transition in $BaTiO_3$, Raman bands in the region 100 to 300 cm^{-1} are most affected. Therefore, much of our investigation will be in this region. A closer view of Raman band at 152 and 234 cm^{-1} is presented in Fig. 6(a)–(d). It is clear from the Fig. 6(a)–(d) that Raman band near 152 cm^{-1} consist of two sub-bands centered at 140 and 160 cm^{-1}. The low frequency mode near 140 cm^{-1} does not exist in pure $BaTiO_3$. The presence of low frequency modes were reported in modified $BaTiO_3$ ceramics but with somewhat inconsistent clarification. For example, Shimazu *et al.*[70] ascribed them to acoustic modes presented at zone centre due to inherent disorder in the system, whereas Puli *et al.*[71] considered it as A(TO_1) mode with low-frequency shift. Moreover, the asymmetric band near 234 cm^{-1} (Fig. 6(a)–(d)) also shows high and low frequency shoulder at 190 and 272 cm^{-1}.

To understand the ZT doping effects on BCZT–*x*ZT, the quantitative analysis of bands at 160 and 234 cm^{-1} was carried out by de-convoluting peaks using Lorentzian function. The best fitted peaks are presented by dotted lines in Fig. 6(a)–(d). The peaks for sub-band are marked by number 1 to 5 (Fig. 6(a)–(d)). The peak number "1" and "2" corresponds to bands at 140 and 160 cm^{-1}. The peaks "3", "4", and "5" corresponds to bands at 190, 234, and 272 cm^{-1}. It is clear from the Fig. 3(a) and (b) that the height of peak "2", "3", and "4" is decreasing and of "1" and "5" is increasing with increase in ZT content. The most noticeable change is considerable fall in the intensity of peak number "3", *i.e.*, band at 190 cm^{-1}.The

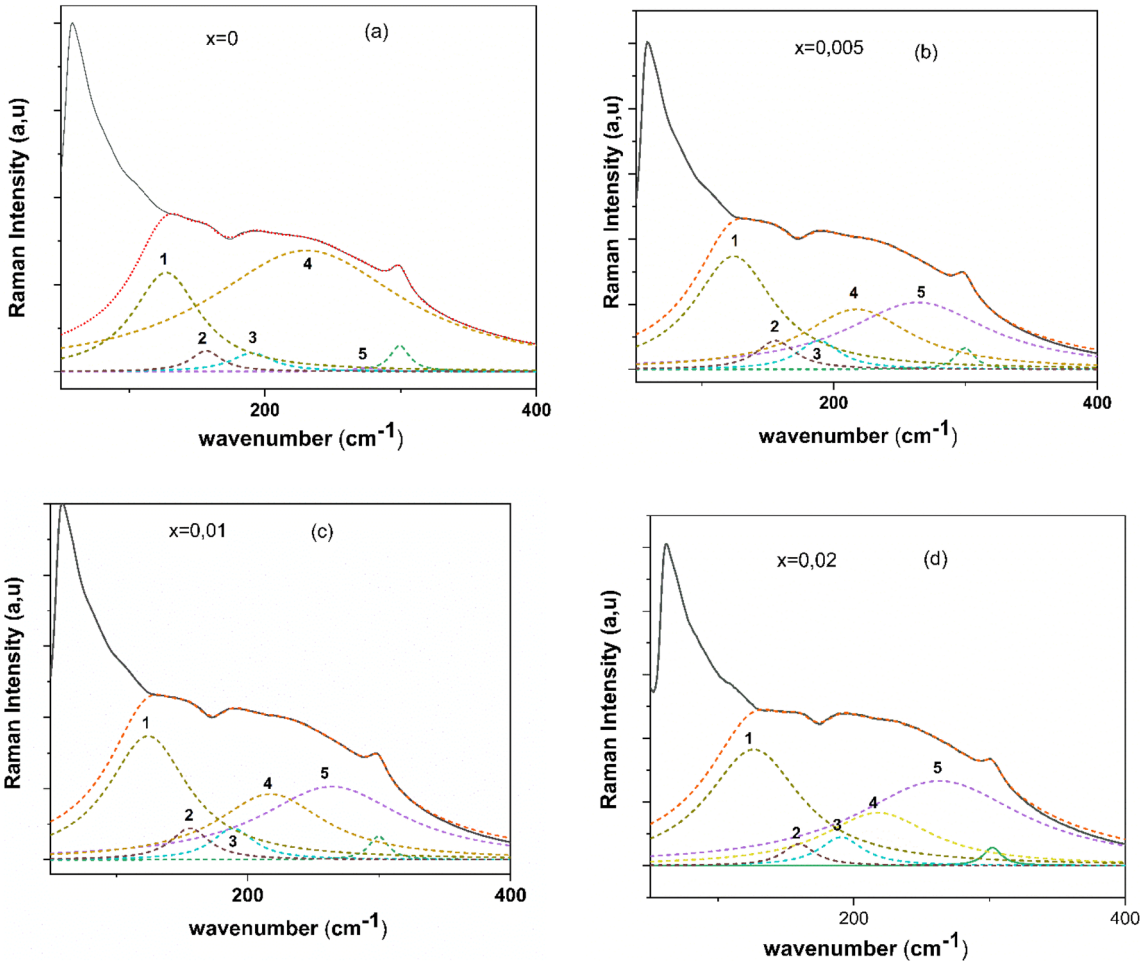

Fig. 6 (a–d) Room temperature Raman spectra of BCZT–xZT in the range (a) 50 to 300 cm^{-1} along with spectra de-convolution.

vibration band near 190 cm^{-1} was assigned to $A(LO_1)$ mode by Xiao *et al.*.[72] The temperature dependent Raman investigation of $BaTiO_3$ reveals that $A(LO_1)$ mode is more prominent in rhombohedral or orthorhombic phase and it vanished for tetragonal phase.[72,73] Another interesting feature of Fig. 6(a)–(d) is presence of modes at 234 and 272 cm^{-1}. The lattice dynamics analysis of $BaTiO_3$ elucidate that there is only one vibration mode,[74] *i.e.*, $A(TO_2)$ between 200 and 280 cm^{-1}. For orthorhombic phase the $A(TO_2)$ mode has vibration frequency near 234 cm^{-1} and it shifts to 272 cm^{-1} for tetragonal phase.[73] Based on our observations on $A(LO_1)$ and $A(TO_2)$ mode, it is inferred that BCZT–xBZT has co-existence of tetragonal and orthorhombic phase at room temperature. More importantly, the intensity variation of peaks "3", "4", and "5" further indicate that fraction of tetragonal phase increases with increase in ZT content. These results are in concurrence with the structural analysis on same system.[75]

The temperature dependent Raman spectra are shown in Fig. 7(a)–(d). The temperature range of interest was from 273 to 333 K as it covers orthorhombic-to-tetragonal phase transition. Although, we did measurements in the temperature range of 273 to 323 K with 5 K step, data was presented for every 10 K in the range 323 to 413 K for sake of clarity. The evolution of Raman spectra with temperature shows some interesting changes. As temperature is increased the bands at 297, 512, and 716 cm^{-1} do not show frequency shift but broadened. The broadening of bands indicates that the Raman selection rule is relaxed ascribed to the disorder in the positions of the Ti/Zr/Ta/Zn atoms in the unit cells of the polycrystalline samples. The asymmetric band near 542 cm^{-1} show reasonable change in the line-shape due to emergence of weak band at 468 cm^{-1} [$E(TO_4)$/$E(LO_3)$/$A(LO_2)$] and significant broadening at higher temperature. With increase in temperature, the sharpness of dip at 180 cm^{-1} weakens reasonably. The weakening of interference dip at 173 cm^{-1} is an indication of reduced coupling between A(TO) modes.[76] The two major changes observed in Raman spectra are: first, a sudden increase in the frequency of $A(TO_2)$ mode from 234 to 272 cm^{-1} was observed. This increase in frequency occur near 308 K for $x = 0$ and 0.05. Here we have presented the closer view $A(TO_2)$ mode at two temperatures in vicinity of orthorhombic-to-tetragonal phase transition. Second, the peak height of $A(LO_1)$ mode at 190 cm^{-1} decreases with increase in temperature. The decrease in the intensity of $A(LO_1)$ mode with temperature reveals that system moves from orthorhombic to tetragonal, as mentioned above. The observed frequency change of $A(TO_2)$ mode for $x = 0$ and $x = 0.005$ are

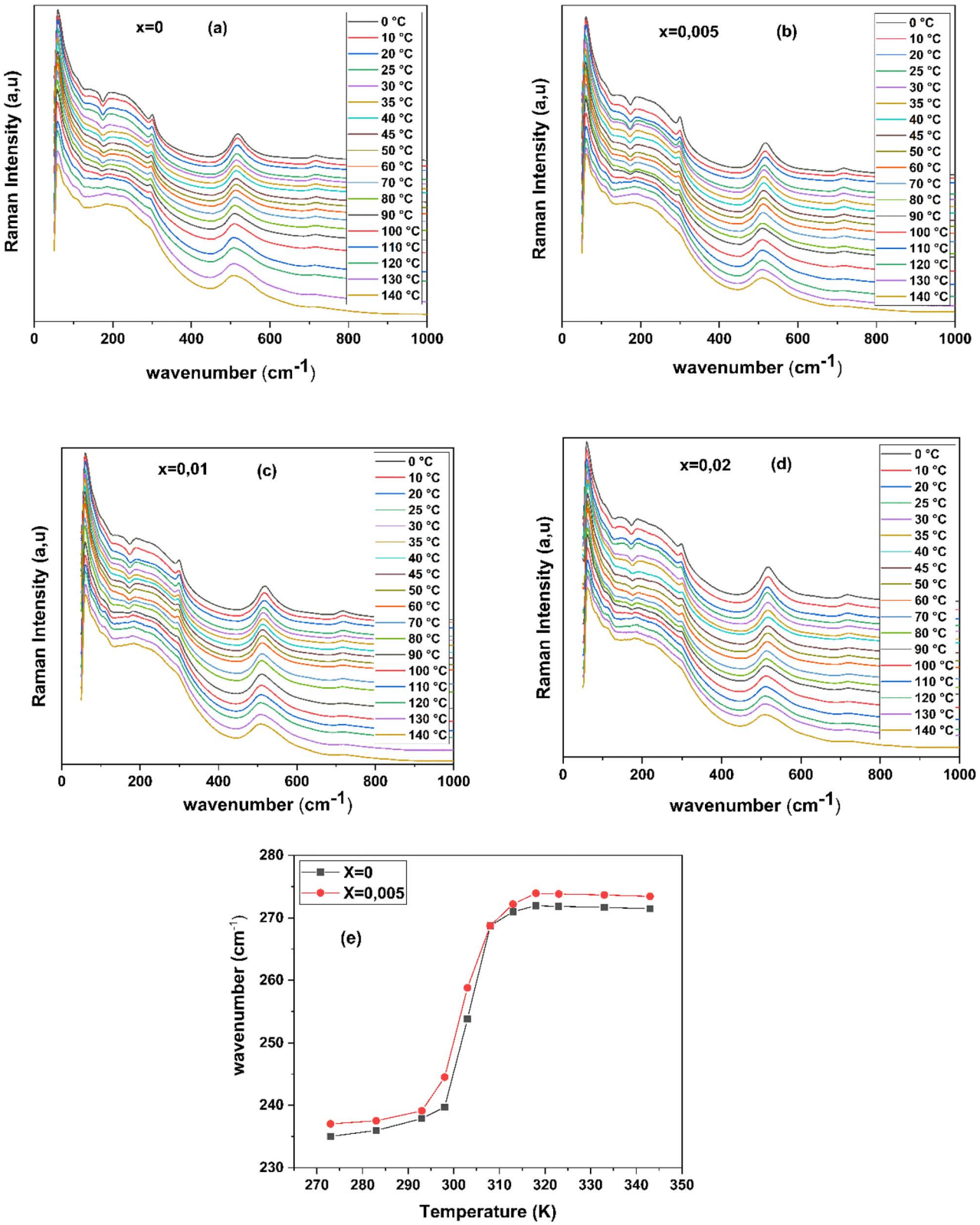

Fig. 7 (a–d) Temperature evolution of Raman spectra of BCZT–xZT in vicinity of orthorhombic-to-tetragonal phase transition during heating and (e) frequency of A(TO_2) mode as a function of temperature.

presented in Fig. 7(e). It is clear from the figure that frequency of A(TO_2) mode almost constant a lower temperature, it increases rapidly from 234 to 272 cm^{-1} in the temperature range of 308 for $x = 0$ and 0.05. With further increase in the temperature the frequency of A(TO_2) mode decreases gradually. Both these results are in agreement with the temperature

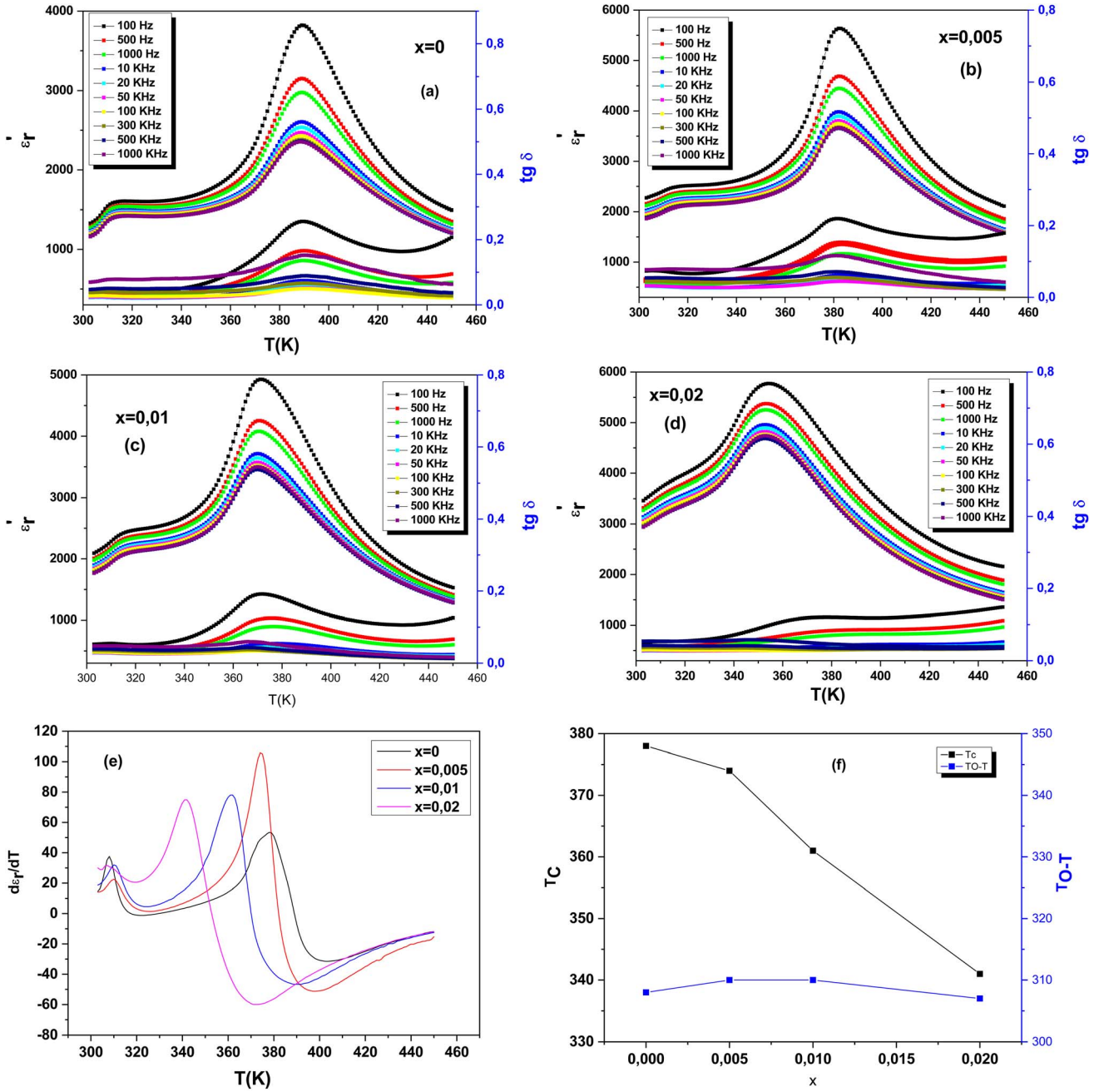

Fig. 8 (a)–(d) Temperature dependence of the dielectric constant of BCZT–*x*BZT ceramics: (a) $x = 0$, (b) $x = 0.005$, (c) $x = 0.01$, (d) $x = 0.02$; (e) the derivate of the dielectric constant as a function of temperature for each composition; (f) phase diagram of BCZT–*x*ZT based on the present dielectric measurements.

dependent Raman study on pure $BaTiO_3$.[73] It is known that $BaTiO_3$ based systems with orthorhombic structure have $A(TO_2)$ mode near 230 cm^{-1} and for tetragonal structure it is shifted near 265 cm^{-1}.[73]

However, we have observed the presence of peak at 267 cm^{-1} even in orthorhombic phase, $(Ba_{0.95}Ca_{0.05})(Zr_{0.05}Ti_{0.95})O_3$ is having an orthorhombic structure as clear from above and from previous studies.[75] The presence of Raman band at 267 cm^{-1} was observed by Osada *et al.*[77] in orthorhombic phase of $BaTiO_3$ and they attributed it to the splitting of $A(TO_2)$ mode due to strain fields at domain walls. More importantly, the mode at 267 cm^{-1} was observed only at domain boundaries. The material under investigation, *i.e.*, $(Ba_{0.95}Ca_{0.05})(Zr_{0.05}Ti_{0.95})O_3$, is a normal ferroelectric below 400 K and have randomly oriented domain at lower temperatures. Therefore, we believe that at lower temperature, *i.e.*, below temperature range of orthorhombic and tetragonal phase co-existence, the presence Raman peak at 267 cm^{-1} is due to splitting of $A(TO_2)$ mode by strain fields at domain walls,[77] as mentioned above. Interestingly, the split mode is observed exactly at the same frequency

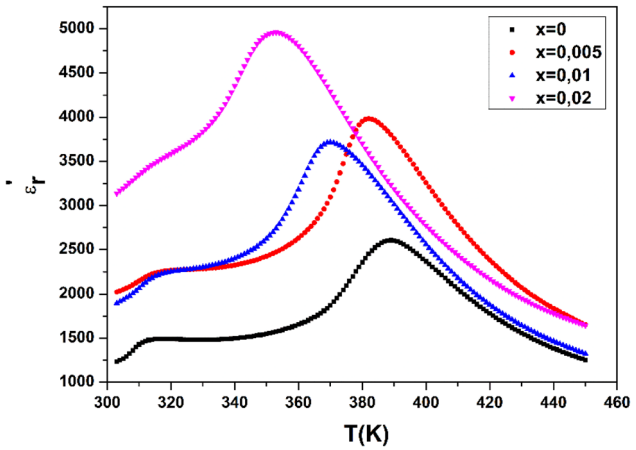

Fig. 9 Temperature dependence of the dielectric properties at 1 kHz for the BCZT–xZT ceramics.

as of A(TO_2) mode in tetragonal phase. Therefore, it can be conjectured that domain walls may have tetragonal structure. However, the two strongest Raman modes, at 512 cm^{-1} (A/E(TO)) and 716 cm^{-1} (A/E(LO)) remain in the cubic phase, this can be related to the existence of ferroelectric clusters or polar nano-regions (PNRs).[78–80]

The temperature and frequency variations of the dielectric constant of BCZT–xZT are shown in Fig. 8(a)–(d). To determine the phase transitions, the curve of the differential dielectric constant ($\partial\varepsilon_r/\partial T$) as a function of temperature,[81,82] presented in Fig. 8(e), shows two obvious peaks are detected around 389 K corresponds to the ferroelectric–paraelectric phase transition from tetragonal phase to cubic phase (T_c) and 313 K corresponds to the ferroelectric–ferroelectric phase transition from orthorhombic phase to tetragonal phase (T_{O-T}) at $x = 0$.

In Fig. 8(f), a simplified phase diagram based on our dielectric measurements shows that a small amount of BZT ($x = 0.005$), slightly shifts the temperature of the orthorhombic–tetragonal (T_{O-T}) phase transition peaks towards a high temperature but almost unchanged. However, when the BZT content increases ($x \geq 0.020$), the T_{O-T} peaks shift to low temperatures and the T_c peaks obviously decrease.

Temperature dependence of the dielectric properties for the BCZT–xZT ceramics ($x = 0$, 0.005, 0.01, 0.02) measured at 10 kHz is shown in Fig. 9. With the addition of ZT, the dielectric constant peak becomes broader and weaker, indicating that the existence of the diffuse phase transition behavior. As we know, the dielectric permittivity of the ferroelectric above the Curie temperature should obey the Curie Weiss law:

$$1/\varepsilon_r = \frac{(T - T_{CW})}{C}$$

where ε_r is the dielectric constant; C is the Curie Weiss constant; T_{CW} is the Curie Weiss temperature; T is the temperature, which is higher than the T_{CW}. Inverse dielectric constant at 10 kHz as a function of temperature for the BCZT–xZT ceramics is shown in Fig. 10(a)–(d). T_M is the peak temperature of the temperature dependence of dielectric constant. T_B is the initial temperature

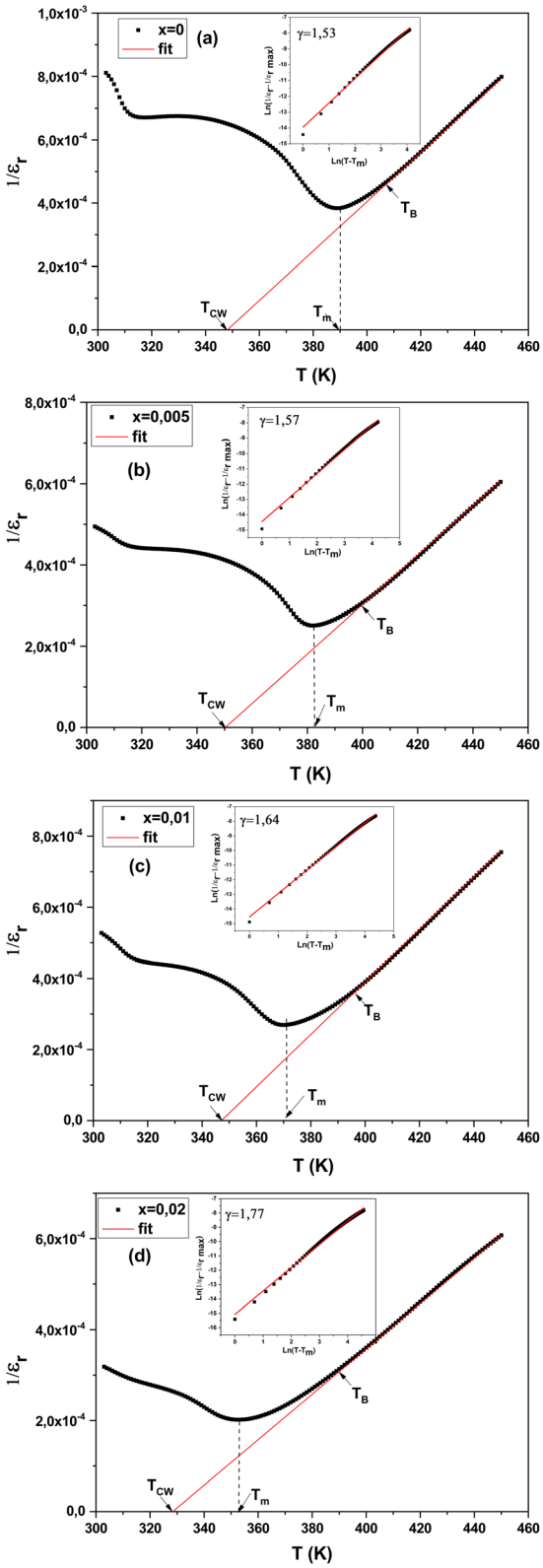

Fig. 10 Inverse dielectric constant at 1 kHz as a function of temperature for the BCZT–xZT ceramics. The inset shows the $\log\left(\frac{1}{\varepsilon_r} - \frac{1}{\varepsilon_m}\right)$ against $\log(T - T_m)$ at 1 kHz.

Table 2 The Curie Weiss temperature (T_{CW}), the initial temperature which the dielectric constant begins to obey Curie Weiss law (T_B), the peak temperature of the temperature dependence of dielectric constant (T_M), the deviation from the Curie–Weiss law (ΔT_M), and the diffuseness coefficient (γ) for the BCZT–xZT ceramics

x	T_{CW}	T_B	T_M	ΔT_M	γ	P_r	P_s	E_c
0	348	405	390	57	1.53	6.91	8.97	6.9
0.005	350	399	382	49	1.57	7.59	10.36	7.9
0.01	347	396	371	49	1.64	6.33	8.51	7.47
0.02	328	389	353	61	1.77	5.24	8.26	6.61

which the dielectric constant begins to obey Curie Weiss law. The deviation from the Curie–Weiss law can be described by ΔT_M as follows:

$$\Delta T_M = T_B - T_M$$

Table 2 lists the results of T_{CW}, T_B, T_M and ΔT_M for the BCZT–xZT ceramics. The value of ΔT_M increases with ZT addition, indicating that the ZT doped BCZT ceramics need higher temperature to make ferroelectric–paraelectric phase transition completely than pure BCZT ceramics after above the T_M.[83]

Uchino and Nomura[84] had proposed a modified empirical expression to further study the diffuse phase transition.

$$\frac{1}{\varepsilon_r} - \frac{1}{\varepsilon_m} = (T - T_m)^{\gamma}$$

where C is the Curie Weiss constant; the γ is the diffuseness coefficient and the value of γ is between 1 and 2. The limiting value $\gamma = 1$ is for the normal ferroelectrics and $\gamma = 2$ is for ideal relaxor ferroelectrics. Fig. 11 shows the logarithmic plots of this equation for all samples. The value of γ can be determined by the slope of fitting line. The γ value increases gradually from 1.53 to 1.77 with increasing ZT content, describing a relaxor ferroelectric feature for all samples of BCZT–xZT.[84]

Fig. 12 shows the relative dielectric constant ε_r at room temperature (100 Hz) and piezoelectric coefficient d_{33} of the BCZT–xZT ceramics. The composition dependence of piezoelectric properties (d_{33}) get maximum value of 297 pC N^{-1} at $x = 0.005$. It was thought that the observed high piezoelectric properties should be attributed to the first-order phase transition near room temperature which is the origin of the coexistence of tetragonal and orthorhombic phases.[85–87] According to Table 1 and Fig. 4, BCZT–0.005ZT has the highest piezoelectric coefficient compared to other compositions, which may be due to the highest density and particle size which was considered to be at the origin of this phenomenon.[83,87] It is evident that the grain size as well as density improvements occur with the ZT content in (1 − x)BCZT–xZT. This is an essential feature as $BaTiO_3$-based materials with grain size ≥10 μm exhibit better ferroelectric and piezoelectric properties.[88] In general, piezoelectric materials with higher grain size display larger domains with thinner domain walls whereas materials with lower grain size possess smaller domains having thicker domain walls which make domain reorientation more difficult and thus degrades piezoelectric response.[89,90] Therefore, it is considered that the piezoelectric materials with larger grain size show improved domain movement response to an applied external stress or electric field.[89,90] Alternatively, dielectric, ferroelectric, and piezoelectric properties can be improved with proper care during synthesis. For example, uniform and higher sintering temperature helps to fully grow the grains so that the materials become denser and pores-free microstructures which are beneficial to enhance the electrical, dielectric, and piezoelectric properties.[89,91,92]

An interesting phenomenon was found: by fitting the XRD patterns, the full-width at half maxima (FWHM) of the diffraction peaks at (100), (110), (111), and (200) was obtained and is shown in Fig. 13. The FWHM increased first and then decreased with the doping of BZT ions, and reached their maximum values at $x = 0.005$. The largest FWHM, for $x = 0.005$ was possibly related to large lattice distortions and structure asymmetry. With the corresponding better piezoelectric and electrical

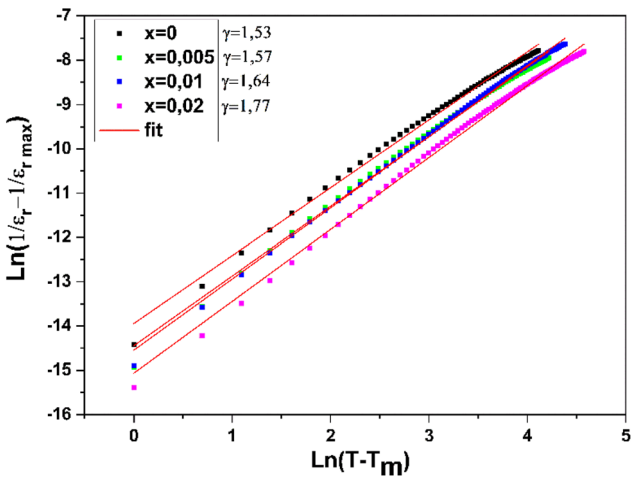

Fig. 11 The log$\left(\frac{1}{\varepsilon_r} - \frac{1}{\varepsilon_m}\right)$ against log($T - T_m$) at 1 kHz for BCZT–xBZT ceramics.

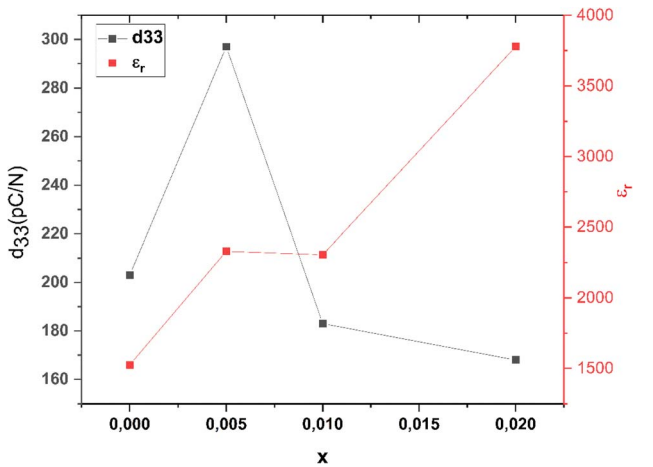

Fig. 12 The relative dielectric constant ε_r at room temperature (100 Hz) and piezoelectric coefficient d_{33} of the BCZT–xZT ceramics.

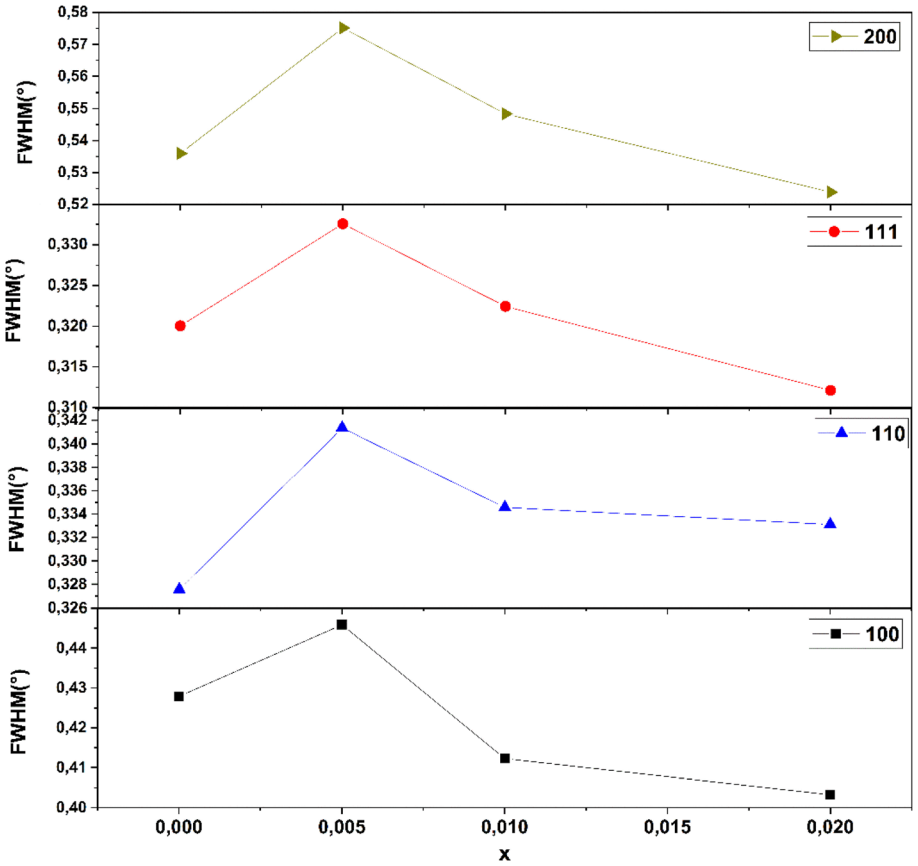

Fig. 13 FWHM for the (100), (110), (111) and (200) diffraction peaks of BCZT–ZT ceramics from the Rietveld refinement.

properties obtained at $x = 0.005$, it may be suggested that large lattice distortions favor these properties.[93]

Considering the high piezoelectric performance at $x = 0.005$, it was not difficult to conclude that this was beneficial to the improvement of piezoelectricity. After ZT ions entered the lattice sites, it is believed that their influences mainly occurred in the following two aspects: firstly, the substitution of ZT ions enhanced the octahedral tiling of TiO_6, resulting in a nonuniform lattice distortion. The size mismatch between ZrO_6 and TiO_6, and the local-structure heterogeneity were the important reasons for the occurrence of local random strain, which further promoted polarization rotation and an enhanced piezoelectric effect. Secondly, the large lattice distortion directly enhanced the local displacement of B-site ions. The ratio of the C to a lattice constants of T phase are summarized in Fig. 14. The maximum (c/a) obtained at $x = 0.005$. Considering the phase fraction and c/a, the highly tetragonal structure was conducive to the displacement enhancement of B-site ions, which enhances the piezoelectric response. This view coincided with the results on lattice parameter expansion obtained from the Rietveld refinement results and this mechanism was expected to be applicable to other piezoelectric materials.[94]

Fig. 15 shows the P–E loops of the BCZT–xZT ceramics measured at 15 Hz at room temperature, being typical ferroelectric polarization hysteresis loops for all ceramic samples. The effect of ZT concentration dopant to the remnant polarization P_r, spontaneous polarization P_s and the coercive field E_c is shown in Table 2. It could be seen that the pure BCZT ceramics exhibited a worse ferroelectric polarization hysteresis loop, and the P–E loops became ameliorative with increased x. E_c increased initially until $x = 0.005$–7.9 kV cm^{-1}, then subsequently doped at x = 0.02–6.61 kV cm^{-1}. This decreases

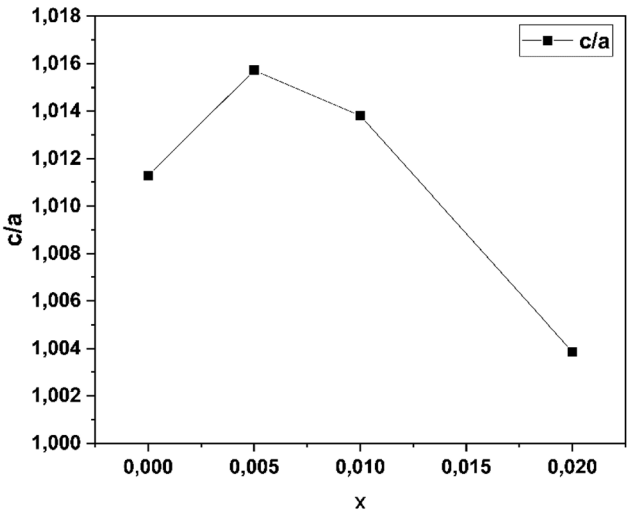

Fig. 14 c/a and α of BCZT–ZT ceramics from the Rietveld refinement.

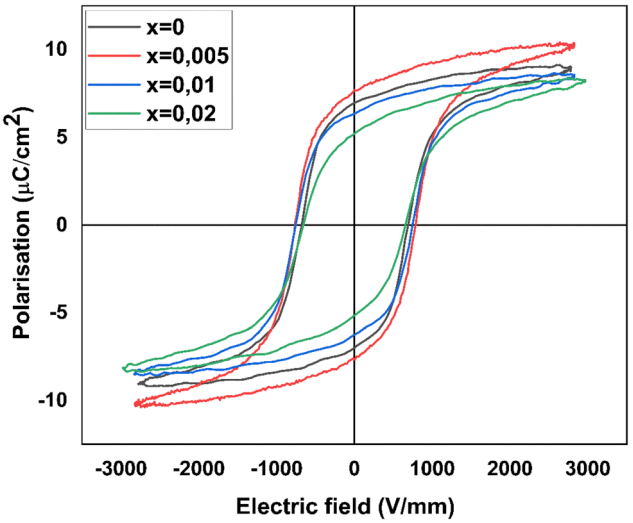

Fig. 15 Polarization–electric field (*P*–*E*) hysteresis loops of the BCZT–*x*ZT ceramics.

indicates that the BCZT–*x*ZT ceramics become more and more "soft".[95] Besides, P_r increased initially, reaching the maximum value at $x = 0.005$–7.59 μC cm^{-2}, and then decreased until $x = 0.02$–5.24 μC cm^{-2}. The results of the coercive field (E_c) showed that the Zn^{2+}/Ta^{5+} doped BCZT ceramics became softer and the ferroelectric properties strongly depended on Zn^{2+} and Ta^{5+} content. Distinctly, the sample with $x = 0.005$ had the largest P_r, suggesting that the increase oxygen vacancies would pin the domain to switch. It was well known that high P_r and low E_c might be ascribed to the coexistence of orthorhombic and tetragonal phases. Generally speaking, large remnant polarization usually facilitated the piezoelectric properties of the ceramics.[96]

4. Conclusions

Lead-free $(1 - x)$BCZT–*x*ZT ($x = 0.00$, 0.005, 0.01, and 0.02) electroceramics were successfully synthesized using solid-state reaction method. The structure, phase, microstructure, dielectric, ferroelectric, piezoelectric, and electrostrictive properties of $(1 - x)$BCZT–*x*ZT have all been thoroughly investigated as a function of variable composition (x). The XRD and Rietveld refinement analyses confirmed the formation of a perovskite structure without the presence of any impurity phases, indicating that Ca^{2+}, Zr^{4+}, Zn^{2+} and Ta^{5+} had effectively diffused into the $BaTiO_3$ lattice. SEM analyses showed the development of a dense microstructure with grains that ranged in size from 11.31 μm to 20.54 μm. Studies using XRD, Rietveld refinement, Raman and dielectric measurements validate and confirm that the crystal symmetry of the orthorhombic (O, *Amm*2) and tetragonal (T, *P*4*mm*) mixed phase in the $(1 - x)$BCZT–*x*ZT materials. When x increases, the ceramics experienced a series of phase transitions, and the c/a ratio of the T phase increased first and then decreased. When the c/a of the tetragonal phase reaches its maximum value, the ceramic with $x = 0.005$ has the best piezoelectricity ($d_{33} \sim 297$ pC N^{-1}).The ceramic with $x = 0.005$ exhibits the optimum piezoelectric and ferroelectric properties *i.e.*, remnant polarization ($P_r = 7.58$ μC cm^{-2}), spontaneous polarization ($P_s = 10.25$ μC cm^{-2}) and piezoelectric coefficient ($d_{33} = 297$ pC N^{-1}), showing the potential possibilities for lead-free piezoelectric application. This research can contribute to the understanding of BCZT ceramics, which improves dielectric, piezoelectric and ferroelectric properties with elements doping and provides an approach to design high-performance lead-free piezoelectric ceramics.

Data availability

The data that support the findings of this study are openly available within the article.

Conflicts of interest

The authors declare that they have no known competing financial interests or personal relationships that could have appeared to influence the work reported in this paper.

Acknowledgements

The authors would like to thank Dr Slimani Ahmed, Sorbonne University, Abu Dhabi for the Scanning Electron Microscopy analysis.

References

1 B. Jaffe, W. R. Cook and H. Jaffe, *Piezoelectric Ceramics*, Academic Press, New York, 1971. DOI: 10.1016/0022-460X(72)90684-0.
2 G. H. Haertling, Ferroelectric ceramics: history and technology, *J. Am. Ceram. Soc.*, 1999, **82**, 797–818.
3 J. Rodel, W. Jo, K. T. P. Seifert, E. M. Anton, T. Granzow and D. Damjanovic, Perspective on the Development of Lead-free Piezoceramics, *J. Am. Ceram. Soc.*, 2009, **92**, 1153, DOI: 10.1111/j.1551-2916.2009.03061.x.
4 S. J. Zhang, R. Xia and T. R. Shrout, Piezoelectric properties in perovskite $0.948(K_{0.5}Na_{0.5})NbO_3$-$0.052LiSbO_3$ lead-free ceramics, *J. Appl. Phys.*, 2006, **100**, 104108, DOI: 10.1063/1.2382348.
5 T. Takenaka, H. Nagata and Y. Himura, Current Developments and Prospective of Lead-Free Piezoelectric Ceramics, *Jpn. J. Appl. Phys.*, 2008, **47**, 3787, DOI: 10.1143/JJAP.47.3787.
6 Y. Choi, T. Hoshina, H. Takeda, T. Teranishi and T. Tsurumi, Effects of oxygen vacancies and grain sizes on the dielectric response of $BaTiO_3$, *Appl. Phys. Lett.*, 2010, **97**, 212907, DOI: 10.1063/1.3508947.
7 R. Clarke, *J. Appl. Crystallogr.*, 1976, **9**, 335.
8 D. Berlincourt and H. H. A. Krueger, Dependence of the Ratio of Piezoelectric Coefficients on Density and Composition of Barium Titanate Ceramics, *Phys. Rev.*, 1957, **105**, 56, DOI: 10.1103/PhysRev.105.56.
9 H. Takahashi, Y. Numamoto, J. Tani, K. Matsuta, J. Qiu and S. Tsurekawa, *Jpn. J. Appl. Phys.*, 2006, **45**, L30.

10 Z. Yu, C. Ang, R. Guo and A. S. Bhalla, *J. Appl. Phys.*, 2002, **92**, 1489.
11 W. Li, Z. Xu, R. Chu, P. Fu and G. Zang, *Braz. J. Phys.*, 2010, **40**, 353.
12 G. Singh, V. S. Tiwari and P. K. Gupta, Thermal stability of piezoelectric coefficients in (Ba1−xCax)(Zr0.05Ti0.95)O3: A lead-free piezoelectric ceramic, *Appl. Phys. Lett.*, 2013, **102**, 162905, DOI: **10.1063/1.480297**.
13 W. Liu and X. Ren, Large piezoelectric effect in Pb-free ceramics, *Phys. Rev. Lett.*, 2009, **103**, 257602.
14 H. L. Wang, F. F. Zhang, Y. Chen, C. T. Huang, X. Y. Wang, X. J. Wu, Y. L. Chen, Y. G. Xu, S. Y. Guan, J. G. Zhu, Q. Chen and J. Xing, *Ceram. Int.*, 2021, **47**, 12284–12291.
15 L. F. Zhu, B. P. Zhang, S. Li and G. L. Zhao, *J. Alloys Compd.*, 2017, **727**, 382–389.
16 C. C. Li, B. Xu, D. B. Lin, S. J. Zhang, L. Bellaiche, T. R. Shrout and F. Li, *Phys. Rev. B*, 2020, **101**, 140102.
17 Q. Liu, Y. C. Zhang, J. Gao, Z. Zhou, H. Wang, K. Wang, X. W. Zhang, L. T. Li and J. F. Li, *Science*, 2018, **11**, 3531–3539.
18 P. Li, J. W. Zhai, B. Shen, S. J. Zhang, X. L. Li, F. Y. Zhu and X. M. Zhang, *Adv. Mater.*, 2018, **30**, 1705171.
19 L. Wang, S. D. Sun, H. J. Luo, Y. Ren, H. Liu, X. R. Xing and J. Chen, *J. Mater. Chem. A*, 2021, **9**, 2367–2374.
20 N. Zhang, X. Lv, X. X. Zhang, J. Lyu, S. W. Yang and J. Wu, *J. Mater. Sci. Technol.*, 2022, **115**, 189–198.
21 K. B. Xi, Y. L. Li, Y. Sun, C. Li, Z. Q. Li, N. Vetri, Z. S. Zheng, C. Yang, D. D. Wang and P. W. Jia, *J. Am. Ceram. Soc.*, 2022, **106**, 466–475.
22 Y. J. Shi, X. Y. Dong, K. Y. Zhao, W. W. Yang, K. Zhu, R. Hu, H. R. Zeng, B. Shen and J. W. Zhai, *ACS Appl. Mater. Interfaces*, 2021, **13**, 14385–14393.
23 M. Deluca and A. Gajovic, Raman Spectroscopy of Nanostructured Ferroelectric Materials, in *Nanoscale Ferroelectrics and Multiferroics*, John Wiley & Sons, Ltd, 2016, pp. 325–374.
24 J.-M. Li, X.-L. Zeng and Z.-An Xu, Partial cationic inversion-induced magnetic hardening of densely packed 23-nm-sized nanocrystallite-interacting nickel ferrite electrospun nanowires, *Appl. Phys. Lett.*, 2013, **103**, 232410, DOI: **10.1063/1.4840320**.
25 T. P. Devereaux and R. Hackl, Inelastic light scattering from correlated electrons, *Rev. Mod. Phys.*, 2007, **79**, 175.
26 J.-M. Li, C. H. A. Huan, Y. W. Huan, D. Feng and Z. X. Shen, Magnetic-field-tunable charge carrier localization in sintered polycrystalline $La_{0.75}Ca_{0.25}MnO_3$, *Phys. Rev. B*, 2000, **63**, 024416, DOI: **10.1103/PhysRevB.63.024416**.
27 M. N. Iliev, M. V. Abrashev, J. Laverdière, S. Jandl, M. M. Gospodinov, Y.-Q. Wang and Y.-Y. Sun, Distortion-dependent Raman spectra and mode mixing in RMnO3 perovskites (R = La, Pr, Nd, Sm, Eu, Gd, Tb, Dy, Ho, Y), *Phys. Rev. B: Condens. Matter Mater. Phys.*, 2006, **73**, 064302.
28 N. K. Karan, R. S. Katiyar, T. Maiti, R. Guo and A. S. Bhalla, Raman spectral studies of Zr 4+ -rich BaZr x Ti 1− x O 3 (0.5≱ x ≱1.00) phase diagram, *J. Raman Spectrosc.*, 2009, **40**, 370–375, DOI: **10.1002/jrs.2134**.
29 V. Buscaglia, S. Tripathi, V. Petkov, M. Dapiaggi, M. Deluca, A. Gajovic and Y. Ren, Average and local atomic-scale structure in BaZrxTi(1-x)O3 (x = 0. 10, 0.20, 0.40) ceramics by high-energy x-ray diffraction and Raman spectroscopy, *J. Phys.: Condens. Matter*, 2014, **26**, 65901, DOI: **10.1088/0953-8984/26/6/065901**.
30 V. K. Veerapandiyan, M. Deluca, S. T. Misture, W. A. Schulze, S. M. Pilgrim and S. C. Tidrow, Dielectric and structural studies of ferroelectric phase evolution in dipole-pair substituted barium titanate ceramics, *J. Am. Ceram. Soc.*, 2020, **103**, 287–296, DOI: **10.1111/jace.16713**.
31 N. H. Khansur, U. R. Eckstein, M. Bergler, A. Martin, K. Wang, J.-F. Li, M. R. Cicconi, K. Hatano, K. Kakimoto, D. de Ligny and K. G. Webber, In situ combined stress- and temperature-dependent Raman spectroscopy of Li-doped (Na,K)NbO 3, *J. Am. Ceram. Soc.*, 2022, **105**, 2735–2743, DOI: **10.1111/jace.18269**.
32 I. Coondoo, N. Panwar, S. Krylova, A. Krylov, D. Alikin, S. K. Jakka, A. Turygin, V. Y. Shur and A. L. Kholkin, Temperature-dependent Raman spectroscopy, domain morphology and photoluminescence studies in lead-free BCZT ceramic, *Ceram. Int.*, 2021, **47**, 2828–2838, DOI: **10.1016/j.ceramint.2020.09.137**.
33 N. Luo, S. Zhang, Q. Li, Q. Yan, Y. Zhang, T. Ansell, J. Luo and T. R. Shrout, Crystallographic dependence of internal bias in domain engineered Mn-doped relaxor-PbTiO3 single crystals, *J. Mater. Chem. C*, 2016, **4**, 4568–4576.
34 J. Zeng, K. Zhao, X. Shi, X. Ruan, L. Zheng and G. Li, Large strain induced by the alignment of defect dipoles in (Bi3+, Fe3+) co-doped Pb (Zr, Ti)O3 ceramics, *Scr. Mater.*, 2018, **142**, 20–22.
35 J. Wu, D. Xiao, W. Wu, Q. Chen, J. Zhu, Z. Yang and J. Wang, Role of room-temperature phase transition in the electrical properties of (Ba,Ca)(Ti,Zr)O_3 ceramics, *Scr. Mater.*, 2011, **65**, 771–774.
36 Z. Zhao, X. Li, H. Ji, Y. Dai and T. Li, Microstructure and electrical properties in Zn-doped $Ba_{0.85}Ca_{0.15}Ti_{0.90}Zr_{0.10}O_3$ piezoelectric ceramics, *J. Alloys Compd.*, 2015, **637**, 291–296.
37 T. Qi, I. Grinberg and A. M. Rappe, Correlations between tetragonality, polarization, and ionic displacement in PbTiO3-derived ferroelectric perovskite solid solutions, *Phys. Rev. B: Condens. Matter Mater. Phys.*, 2010, **82**, 134113, DOI: **10.1103/PhysRevB.82.134113**.
38 F. Zeng, Q. Liu, E. Cai, Y. Wang, A. Xue, S. Peng, S. Zhou and Y. Zhu, Relaxor phenomenon of (1-x)$(Ba_{0.85}Ca_{0.15})(Zr_{0.09}Ti_{0.91})O_3$-xTa + 0.6wt.% Li_2CO_3 ceramics with high piezoelectric constant and Curie temperature, *Ceram. Int.*, 2018, **44**, 10677–10684, DOI: **10.1016/j.ceramint.2018.03.098**.
39 Li-F. Zhu, Bo-P. Zhang, L. Zhao and J.-F. Li, High piezoelectricity of $BaTiO_3$-$CaTiO_3$-$BaSnO_3$ lead-free ceramics, *J. Mater. Chem. C*, 2014, **2**, 4764, DOI: **10.1039/c4tc00155a**.
40 K. H. Yoon, J. H. Kim, K. H. Jo, H. I. Song, S. O. Yoon and C. S. Kim, Effect of Ca2+ Ions on Electrical Properties of $Ba_{1-x}Ca_xTi_{0.90}Sn_{0.10}O_3$-0.05Y2O3 Ceramics, *J. Mater. Sci.*, 1988, **23**, 61, DOI: **10.1007/s11664-018-6147-3**.

41 R. D. Shannon, Revised effective ionic radii and systematic studies of interatomic distances in halides and chalcogenides, *Acta Crystallogr., Sect. A: Cryst. Phys., Diffr., Theor. Gen. Crystallogr.*, 1976, **32**, 751–767, DOI: **10.1107/S0567739476001551**.

42 A. Shandilya, R. S. Yadav, A. K. Gupta and K. Sreenivas, Effects of Yb^{3+} ion doping on lattice distortion, optical absorption and light upconversion in Er^{3+}/Yb^{3+} co-doped $SrMoO_4$ ceramics, *Mater. Chem. Phys.*, 2021, **264**, 124441, DOI: **10.1016/j.matchemphys.2021.124441**.

43 M. V. Madhava Rao, Chen-Feng Kao, $(Bi_{0.5}Na_{0.5})_{0.93}Ba_{0.07}TiO_3$ lead-free ceramics with addition of Ga_2O_3, *Phys. B*, 2008, **403**, 3596–3598, DOI: **10.1016/j.physb.2008.05.039**.

44 W. Li, H. Jigong, W. Bai, Xu Zhijun, R. Chu and J. Zhai, Enhancement of the temperature stabilities in yttrium doped (Ba0.99Ca0.01)(Ti0.98Zr0.02)O3 ceramics, *J. Alloys Compd.*, 2012, **531**, 46–49, DOI: **10.1016/j.jallcom.2012.03.110**.

45 L. Zheng, Mu Liu, H. Zhang, Z. Zheng, Z. Wang, H. Cheng, P. Wang, Y. Liu and B. Huang, Fabrication of ZnO Ceramics with Defects by Spark Plasma Sintering Method and Investigations of Their Photoelectrochemical Properties, *Nanomaterials*, 2021, **11**, 2506, DOI: **10.3390/nano11102506**.

46 L.-F. Zhu, B.-P. Zhang, X.-K. Zhao, L. Zhao, P.-F. Zhou and J.-F. Li, *J. Am. Ceram. Soc.*, 2013, **96**, 241.

47 A. K. Kalyani, K. Brajesh, A. Senyshyn and R. Ranjan, Orthorhombic-tetragonal phase coexistence and enhanced piezo-response at room temperature in Zr, Sn, and Hf modified $BaTiO_3$, *Appl. Phys. Lett.*, 2014, **104**, 252906, DOI: **10.1063/1.4885516**.

48 M. Abebe, K. Brajesh, A. Mishra, A. Senyshyn and R. Ranjan, Structural perspective on the anomalous weak-field piezoelectric response at the polymorphic phase boundaries of (Ba,Ca)(Ti,M)O3 lead-free piezoelectrics (M=Zr, Sn, Hf), *Phys. Rev. B*, 2017, **96**, 014113, DOI: **10.1103/PhysRevB.96.014113**.

49 L. Li, J. Deng, J. Chen, X. Sun, R. Yu, G. Liu and X. X. Wire, *Chem. Mater.*, 2009, **21**(7), 1207–1213.

50 R. Verma, A. Chauhan, K. M. Batoo, R. Kumar, M. Hadi and E. H. Raslan, Structural, morphological, and optical properties of strontium doped lead-free BCZT ceramics, *Ceram. Int.*, 2021, **47**, 15442–15457, DOI: **10.1016/j.ceramint.2021.02.110**.

51 C. Han, J. Wu, P. Chaohui, S. Qiao, B. Wu, J. Zhu and D. Xiao, *Ceram. Int.*, 2012, **38**, 6359–6363.

52 A. Watcharapasorn and S. Jiansirisomboon, *Ceram. Int.*, 2008, **34**, 769–772.

53 M. P. Fontana and M. Lambert, Linear disorder and temperature dependence of Raman scattering in $BaTiO_3$, *Solid State Commun.*, 1972, **10**, 1.

54 U. D. Venkateswaran and V. M. Naik, High-pressure Raman studies of polycrystalline, *Phys. Rev. B: Condens. Matter Mater. Phys.*, 1998, **58**, 14256–14260, DOI: **10.1103/PhysRevB.58.14256**.

55 M. Srivastava, B. Kumar, R. Prasad, N. Kumari and S. N. Prasad, Spectral studies of some transition metal chelates with thiolactic anilide and thiolactic-p-toluidide, Part-II, *Asian J. Chem.*, 1999, **11**, 1501–1504, DOI: **10.1002/jrs**.

56 P. Hermet, M. Veithen and P. Ghosez, Raman scattering intensities in $BaTiO_3$ and $PbTiO_3$ prototypical ferroelectrics from density functional theory, *J. Phys.: Condens.Matter*, 2009, **21**, 215901, DOI: **10.1088/0953-8984/21/21/215901**.

57 P. S. Dobal, A. Dixit, R. S. Katiyar, D. Garcia, R. Guo and A. S. Bhalla, Micro-Raman study of $Ba_{1-x}Sr_xTiO_3$ ceramics, *J. Raman Spectrosc.*, 2001, **32**, 147.

58 C. J. Xiao, Z. H. Chi, W. W. Zhang, F. Y. Li, S. M. Feng, C. Q. Jin, X. H. Wang, X. Y. Deng and L. T. Li, The phase transitions and ferroelectric behavior of dense nanocrystalline $BaTiO_3$ ceramics fabricated by pressure assisted sintering, *J. Phys. Chem. Solids*, 2007, **68**, 311–314, DOI: **10.1016/j.jpcs.2006.11.014**.

59 G. Singh, V. Sathe and V. S. Tiwari, Investigation of orthorhombic-to-tetragonal structural phase transition scattering, *J. Appl. Phys.*, 2014, **115**, 044103.

60 S. Liu, L. Zhang, J. Wang, X. Shi, Y. Zhao and D. Zhang, Rapid stability of ferroelectric polarization in the Ca, Ce hybrid doped BaTiO3ceramics, *Sci. Rep.*, 2016, **6**, 1–8, DOI: **10.1038/srep38354**.

61 F. M. Pontes, M. T. Escote, C. C. Escudeiro, E. R. Leite, E. Longo, A. J. Chiquito, P. S. Pizani and J. A. Varela, Characterization of $BaTi_{1-x}Zr_xO_3$ thin films obtained by a soft chemical spin-coating technique, *J. Appl. Phys.*, 2004, **96**, 4386.

62 T. Hoshina, H. Kakemoto, T. Tsurumi, S. Wada and M. Yashima, Size and temperature induced phase transition behaviors of barium titanate nanoparticles, *J. Appl. Phys.*, 2006, **99**, 054311.

63 P. S. Dobal, A. Dixit, R. S. Katiyar, Z. Yu, R. Guo and A. S. Bhalla, Phase transition behavior of $BaZr_xTi_{1-x}O3$ ceramics, *J. Raman Spectrosc.*, 2001, **32**, 69.

64 R. Farhi, M. EI Marssi, A. Simon and J. Ravez, A Raman and dielectric study of ferroelectric ceramics, *Eur. Phys. J. B*, 1999, **9**, 599.

65 A. Slodczyk and P. Colomban, Probing the Nanodomain Origin and Phase Transition Mechanisms in (Un)Poled PMN-PT Single Crystals and Textured Ceramics, *Materials*, 2010, **3**, 5007, DOI: **10.3390/ma3125007**.

66 A. Slodczyk, P. Daniel and A. Kania, *Phys. Rev. B: Condens. Matter Mater. Phys.*, 2008, **77**, 184114.

67 Z. Ž. Lazarević, M. M. Vijatović, B. D. Stojanović, M. J. Romčević and N. Ž. Romčević, Structure study of nanosized La- and Sb-doped $BaTiO_3$, *J. Alloys Compd.*, 2010, **494**, 472.

68 J. Kreisel, P. Bouvier, M. Maglione, B. Dkhil and A. Simon, High-pressure Raman investigation of the Pb-free relaxor $BaTi_{0.65}Zr_{0.35}O_3$, *Phys. Rev. B*, 2004, **69**, 092104.

69 D. Maurya, A. Kumar, V. Petkov, J. E. Mahaney, R. S. Katiyare and S. Priya, Local structure and piezoelectric instability in lead free (1- x)$BaTiO_3$-xA($Cu_{1/3}Nb_{2/3}$)O3 (A=Sr, Ca, Ba) solid solutions, *RSC Adv.*, 2014, **4**, 1283, DOI: **10.1039/c3ra44886**.

70 T. Shimizu, D. Fu, H. Taniguchi, T. Taniyama and M. Itoh, *Appl. Phys. Lett.*, 2012, **100**, 102908.
71 V. S. Puli, A. Kumar, D. B. Chrisey, M. Tomozawa, J. F. Scott and R. S. Katiyar, *J. Phys. D: Appl. Phys.*, 2011, **44**, 395403.
72 C. J. Xiao, Z. H. Chi, W. W. Zhang, F. Y. Li, S. M. Feng, C. Q. Jin, X. H. Wang, X. Y. Deng and L. T. Li, *J. Phys. Chem. Solids*, 2007, **68**, 311.
73 C. H. Perry and D. B. Hall, Temperature Dependence of the Raman Spectrum of $BaTiO_3$, *Phys. Rev. Lett.*, 1965, **15**, 700, DOI: 10.1103/PhysRevLett.15.700.
74 J. D. Freire and R. S. Katiyar, Lattice dynamics of crystals with tetragonal $BaTiO_3$ structure, *Phys. Rev. B: Condens. Matter Mater. Phys.*, 1988, **37**, 2074, DOI: 10.1103/PhysRevB.37.2074.
75 G. Singh, V. S. Tiwari and P. K. Gupta, Evaluating the polymorphic phase transition in calcium-doped Ba(Zr0.05Ti0.95)O3: a lead-free piezoelectric ceramic, *J. Appl. Crystallogr.*, 2013, **46**, 324, DOI: 10.1107/S0021889813000666.
76 S. Y. Kuo, W. Y. Liao and W. F. Hsieh, *Phys. Rev. B: Condens. Matter Mater. Phys.*, 2001, **64**, 224103.
77 M. Osada, M. Kakihana, S. Wada, T. Noma and W. S. Cho, *Appl. Phys. Lett.*, 1999, **75**, 3393.
78 L. H. F. Bijun, L. Xing, L. Xiaobing, D. Jianning and Z. Xiangyong, Temperature-dependent Raman spectra and electrical propertiesof $0.69Pb(Mg_{1/3}Nb_{2/3})O_3$ –0.31PbTiO 3 single crystals, *Appl. Phys. A*, 2016, **122**, 1–9, DOI: 10.1007/s00339-016-0340-0.μ.
79 G. Ramesh, M. S. Ramachandra Rao, V. Sivasubramanian and V. Subramanian, Electrocaloric effect in (1-x)PIN-xPT relaxor ferroelectrics, *J. Alloys Compd.*, 2016, **663**, 444–448, DOI: 10.1016/j.jallcom.2015.11.028.
80 S. Praharaj, D. Rout, S. Anwar and V. Subramanian, Polar nano regions in lead free $(Na_{0.5}Bi_{0.5})TiO_3$-$SrTiO_3$-$BaTiO_3$ relaxors: An impedance spectroscopic study, *J. Alloys Compd.*, 2017, **706**, 502–510, DOI: 10.1016/j.jallcom.2017.02.257.
81 H. Abdmouleh, I. Kriaa, N. Abdelmoula, Z. Sassi and H. Khemakhem, The effect of Zn^{2+} and Nb^{5+} substitution on structural, dielectric, electrocaloric properties, and energy storage density of $Ba_{0.95}Ca_{0.05}Ti_{0.95}Zr_{0.05}O_3$ ceramics, *J. Alloys Compd.*, 2021, **878**, 160355, DOI: 10.1016/j.jallcom.2021.160355.
82 M. Zhou, R. Liang, Z. Zhou, C. Xu, X. Nie and X. Dong, Enhanced Curie temperature and piezoelectric properties of $(Ba_{0.85}Ca_{0.15})(Zr_{0.10}Ti_{0.90})O_3$ lead-free ceramics after the addition of $LiTaO_3$, *Mater. Res. Bull.*, 2018, **106**, 213–219, DOI: 10.1016/j.materresbull.2018.05.036.
83 H. Zhao, W. Ma, J. Guo, X. Zang, P. Miao, M. Ma and F. Zhang, Low temperature sintering and role of room-temperature phase transition in the electrical properties of $(Ba_{0.85}Ca_{0.15})(Zr_{0.10}Ti_{0.90})_{1-x}(Cu_{1/3}Nb_{2/3})_xO_3$ ceramics, *J. Mater. Sci.: Mater. Electron.*, 2018, **29**, 2949–2957, DOI: 10.1007/s10854-017-8225-3.
84 K. Uchino and S. Nomura, Critical exponents of the dielectric constants in diffused phase-transition crystals, *Ferroelectrics*, 1982, **44**, 55–61.
85 Y. Cui, C. Yuan, X. Liu, *et al.*, Lead-free $(Ba_{0.85}Ca_{0.15})(Ti_{0.9}Zr_{0.1})O_3$-$Y_2O_3$ ceramics with large piezoelectric coefficient obtained by low-temperature sintering, *J. Mater. Sci.: Mater. Electron.*, 2013, **24**, 654–657, DOI: 10.1007/s10854-012-0785-7.
86 J. G. Wu, D. Q. Xiao, W. J. Wu, Q. Chen, J. G. Zhu, Z. C. Yang and J. Wang, Composition and poling condition-induced electrical behavior of $(Ba_{0.85}Ca_{0.15})(Ti_{1-x}Zr_x)O_3$ lead-free piezoelectric ceramics, *J. Eur. Ceram. Soc.*, 2012, **32**, 891–898, DOI: 10.1016/j.jeurceramsoc.2011.11.003.
87 P. Wang, Y. X. Li and Y. Q. Lu, Enhanced Piezoelectric Properties of $(Ba_{0.85}Ca_{0.15})(Ti_{0.9}Zr_{0.1})O_3$ Lead-Free Ceramics by Optimizing Calcination and Sintering Temperature, *J. Eur. Ceram. Soc.*, **31**(201), 2005–2012, DOI: 10.1016/j.jeurceramsoc.2011.04.023.
88 X. Liu, Z. Chen, B. Fang, J. Ding, X. Zhao, H. Xu and H. Luo, *J. Alloys Compd.*, 2015, **640**, 128.
89 L.-F. Zhu, B.-P. Zhang, L. Zhao and J.-F. Li, *J. Mater. Chem. C*, 2014, **2**, 4764.
90 Y. Tan, G. Viola, V. Koval, C. Yu, A. Mahajan, J. Zhang, H. Zhang, X. Zhou, N. V. Tarakina and H. Yan, *J. Eur. Ceram. Soc.*, 2019, **39**, 2064.
91 V. Bijalwan, J. Erhart, Z. Spotz, D. Sobola, V. Prajzler, P. Tofel and K. Maca, *J. Am. Ceram. Soc.*, 2021, **104**, 1088.
92 V. Bijalwan, P. Tofel, J. Erhart and K. Maca, *Ceram. Int.*, 2019, **45**, 317.
93 Y. Ma, M. Zhao, D. Zhang, Z. Li, M. Zhang, L. Jin and Y. Yan, Enhanced piezoelectricity in $Pb(Zr_{0.48}Ti_{0.52})O_3$-$Pb(Mn_{1/3}Sb_{2/3})$O3-$Pb(Mg_{1/3}Ta_{2/3})O_3$ ceramics through the synergistic effect of defect engineering and lattice distortion, *J. Alloys Compd.*, 2023, **967**, 171779, DOI: 10.1016/j.jallcom.2023.171779.
94 X. Wang, Yu Huan, S. Ji, Y. Zhu, T. Wei and Z. Cheng, Ultra-high piezoelectric performance by rational tuning of heterovalent-ion doping in lead-free piezoelectric ceramics, *Nano Energy*, 2022, **101**, 107580, DOI: 10.1016/j.nanoen.2022.107580.
95 Z.-hui Chen, Z.-wei Li, C. Fang, J.-hua Qiu, J.-ning Ding, W.-qin Zhu and J.-jun Xu, Dielectric and ferroelectric properties of $Ba_{0.87}Ca_{0.10}La_{0.03}Ti_{1-x}Sn_xO_3$, Lead-free ceramics, *J. Phys. Chem. Solids*, 2017, **111**, 311–316.
96 X. F. Wang, P. F. Liang, X. L. Chao and Z. P. Yang, Polymorphic phase transition and enhanced electrical properties of (Ba0.91Ca0.09-xSrx)(Ti0.92Sn0.08)O3 lead-free ceramics, *Ceram. Int.*, 2014, **40**, 9389–9394, DOI: 10.1016/j.ceramint.2014.02.008.